Rare Met. (2024) 43(4):1407–1434
https://doi.org/10.1007/s12598-023-02573-w

RARE METALS

REVIEW

Recent advances in bioinspired vision systems with curved imaging structures

Ze-Ping He, Xun Han, Wen-Qiang Wu, Zhang-Sheng Xu, Cao-Feng Pan*

Received: 2 April 2023 / Revised: 16 May 2023 / Accepted: 17 May 2023 / Published online: 20 February 2024

Abstract Limited by the planar imaging structure, the commercial camera needs to introduce additional optical elements to compensate for the curved focal plane to match the planar image sensor. This results in a complex and bulky structure. In contrast, biological eyes possess a simple and compact structure due to their curved imaging structure that can directly match with the curved focal plane. Inspired by the structures and functions of biological eyes, curved vision systems not only improve the image quality, but also offer a variety of advanced functions. Here, we review the recent advances in bioinspired vision systems with curved imaging structures. Specifically, we focus on their applications in implementing different functions of biological eyes, as well as the emerging curved neuromorphic imaging systems that incorporate bioinspired optical and neuromorphic processing technologies. In addition, the challenges and opportunities of bioinspired curved imaging systems are also discussed.

Z.-P. He, Z.-S. Xu, C.-F. Pan*
CAS Center for Excellence in Nanoscience, Beijing Key Laboratory of Micro-Nano Energy and Sensor, Beijing Institute of Nanoenergy and Nanosystems, Chinese Academy of Sciences, Beijing 100083, China
e-mail: cfpan@binn.cas.cn

Z.-P. He, Z.-S. Xu, C.-F. Pan
School of Nanoscience and Technology, University of Chinese Academy of Sciences, Beijing 100049, China

X. Han
ZJU-Hangzhou Global Scientific and Technological Innovation Center, School of Micro-Nano Electronics, Zhejiang University, Hangzhou 311200, China

W.-Q. Wu
Institute of Microscale Optoelectronics, Shenzhen University, Shenzhen 518060, China

Keywords Bioinspired; Curved vision system; Compound eye; Chambered eye; Neuromorphic

1 Introduction

The eye is an important organ for the living creatures to perceive the information from the external environment. In fact, over 80% of the information we receive from the outside world is transmitted to the brain through eyes [1]. The human eye is composed of several optical components, including the cornea, lens, and vitreous body, as well as the curved retina that senses light [2]. The camera, considered as an artificial eye, has a similar structure to that of the human eye, consisting of a complex lens system and a planar image sensor. However, there is a striking difference between them in the structure of the photosensitive parts. The curved retina of the human eye can match the curved focal plane caused by the simple lens structure, which is common in biology [3–7]. In contrast, cameras use a flat charge coupled device (CCD) or complementary metal-oxide semiconductor (CMOS) image sensor that requires the introduction of additional optical elements to reduce the tendency of the focal plane towards the curved structure, thus minimizing the focal plane curvature [8]. However, the addition of optical elements increases the mass and volume of the camera and introduces optical aberrations, especially off-axis [9]. To solve the above issues, inspired by biological eyes, curved imaging structures have been applied to commercial imaging systems. The camera with the curved imaging structure simplifies the imaging system, resulting in lighter mass and smaller volume. Additionally, the curved imaging structure can improve the image quality, showing significantly better modulation transfer function (MTF) and relative illumination, especially at the edges of the image field [10–13].

In nature, all living creatures, besides humans, have evolved their own unique visual systems [14–20]. In addition to the same curved image structure, biological eyes vary in shape, size, and composition to realize different functions and adapt to different environments. For example, the compound eyes of insects, made up of thousands of ommatidia on the curved surface, provide an exceptionally wide field of view that is challenging to replicate with traditional flat cameras [21]. Amphibians have a clear view of both water and air, which is essential for amphibious monitoring systems [22]. The different adjustable focusing modes of human and fish eyes are instructive for the zoom of the curved surface imaging system [23, 24]. Since the excellent dynamic imaging ability, the praying mantis with compound eyes can catch insects flying at high speed, having great potential in high-speed imaging and dynamic monitoring [25]. In addition, the neuromorphic data processing function of biological vision enables energy-efficient object recognition, promoting the development of image processing systems [26–28].

After a long period of evolution, creatures in nature have developed eyes with different structures and functions to adapt to different living environments, such as wide field of view, adjustable focus, dynamic imaging, wide spectral response, and amphibious imaging. To achieve miniaturization and multi-functionality, bioinspired vision systems with curved imaging structures have been extensively studied. In this review, we discuss the recent advances in the development of curved imaging systems that mimic the structure and function of biological eyes. We focus on bioinspired vision systems with different functions as well as attempts at implementing neuromorphic processing in curved vision systems. Finally, we present potential challenges and prospects in this research area.

2 Characteristics of biological eyes

Over tens of thousands of years, creatures in different environments have evolved eyes with different structures and functions to meet their survival needs. In this section, we present some basic characteristics of biological eyes, including structures, functions, and nervous systems.

2.1 Structures

Driven by large amounts of data and highly demanding tasks, the evolution of biological eyes went through four stages (Fig. 1a): nondirectional photoreception, directional photoreception, low-resolution vision, and high-resolution vision. Typical of non-directional photoreception, photoreceptor cells without membrane stacking and proximity to screening pigments or other light-shielding structures can only sense light. Planarian larvae with pigmented cells can judge the direction of light. Box jellyfish has less photoreceptor cells in the retina, resulting in low-resolution vision. Vertebrates and arthropods possess high-density photoreceptor cells and good optical focusing systems for high-resolution vision. Biological eyes have become increasingly complex and powerful [29].

High-resolution biological eyes have two main structures: chambered eyes and compound eyes. Chambered eyes are mainly found in vertebrates and cephalopods. Chambered eyes in different creatures which differ slightly in structure and shape share the basic structure of a curved retina, a lens structure for focusing light, and light management components for accommodation and adaptation (Fig. 1b) [4, 30, 31]. Light entering the eye is focused by the lens, and then it is adjusted by light management components to project onto the retina, which could stimulate the photoreceptor cells to generate electrical signals that are transmitted to the brain for image formation [32].

The eyes of insects, crustaceans, and other arthropods are mostly compound eyes. The compound eye is made up of thousands of ommatidia on a curved surface. A typical ommatidium in compound eye is an independent photoreceptor unit containing a faceted lens, a cone, a rhabdom, and photoreceptor cells (Fig. 1c) [33]. Light entering the ommatidia converges on the light-sensitive areas under the action of the cornea and cone. Then the rhabdom converts the light signal into an electrical signal to produce visual perception [21]. These highly integrated photoreceptor units of the compound eye allow dragonflies and other appositional compound insects to simultaneously perceive images in different directions. Besides the appositional compound eye, another type of compound eye is the superposition eye (Fig. 1c). The superposition eye focuses all incoming light onto a photosensitive area and only one image can be obtained. The superposition eye is therefore highly sensitive, with receptors that receive 100 to 1000 times more light than the positioned eye. The superposition eye is common in nocturnal insects and deep-sea crustaceans [34].

2.2 Functions

In long-term interaction with the environment, creatures have evolved eyes with different functions, such as wide field of view, adjustable focus, deep depth of view, dynamic imaging, wide spectral response, amphibious imaging, and so on.

As a typical chambered eye, the structure of the human eye is simple and compact, consisting essentially of a

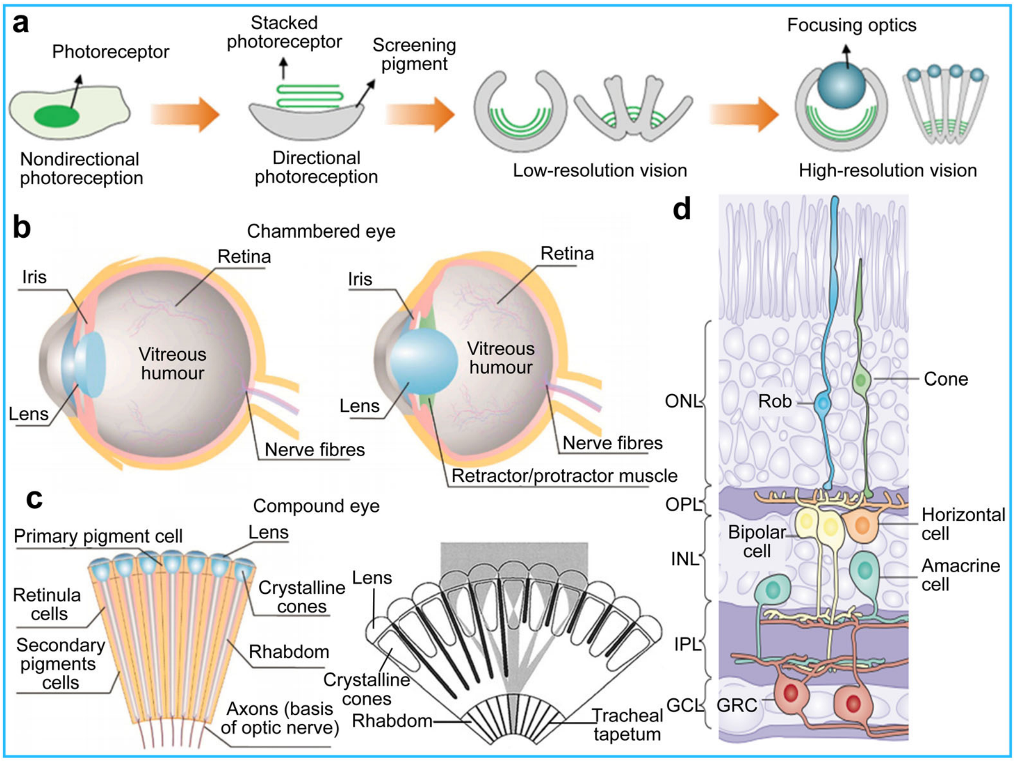

Fig. 1 **a** Four stages of eye evolution: nondirectional photoreceptors, directional photoreception, low-resolution vision, and high-resolution vision. Reproduced with permission from Ref. [29]. Copyright 2013, Cambridge University Press. **b** Schematic illustration of chambered eye (human eye, left; aquatic eye, right); **c** schematic illustration of compound eye (apposition compound eye, left; superposition eye, right). Reproduced with permission from Ref. [31]. Copyright 2021, Elsevier. Reproduced with permission from Ref. [34]. Copyright 2014, Institute of Zoology, Chinese Academy of Sciences. **d** Schematic representation of retinal cells. Reproduced with permission from Ref. [45]. Copyright 2014, Nature Publishing Group

cornea, an iris that controls the intensity of incident light, an adjustable lens, a hyaline colloidal vitreous body, and a curved retina for light detection (Fig. 1b) [2]. In particular, the curved retina can directly compensate for the aberration of the curved focal plane, giving the human eye the function of a wide field of view [31]. In addition, three types of cones in the retina respond to red, green, and blue light, providing a wide spectral response with wavelengths ranging from 380 to 780 nm [35, 36]. To view objects at different distances, the lens in the human eye change their curvature under the action of the ciliary muscles. This allows light from objects at different distances to be focused on the retina [23]. In addition, more advanced focusing functions in biological eyes can change not only the curvature of the lens, but also the curvature of the cornea and the distance between the lens and the cornea. For example, high-flying eagles can quickly adjust their eyes' focus as they descend to the ground, ensuring accurately capture prey [37].

Unlike the asymmetrical lens of land animals, the lens of aquatic fish are symmetrical and spherical (Fig. 1b). This is owing to that the refractive index of water and the biological fluids that make up the eyes are very similar. The cornea of land animals provides the main refractive power of the visual system in the atmospheric environment. In contrast, the cornea of fish cannot focus light in water and all the refractive power is concentrated in the lens, giving rise to the spherical lens [4]. This symmetrical lens and retina give fish a wider field of view up to 160° [38]. But the curvature of the spherical lens with incompressible characteristic cannot be changed to adjust refraction. So, fish have evolved an adjustable focusing mode by changing the position of the lens [4].

Compared to chambered eyes, the compound eye has a wider field of view and can theoretically achieve panoramic imaging [39]. However, the compound eye can't change the focal length, so it has evolved the function of deep depth of field to achieve imaging of near and far objects [40, 41]. Another outstanding function of the compound eye is powerful dynamic imaging. When a moving target is encountered, the ommatidia can detect changing light intensity from different directions. Meanwhile, together with a higher refresh rate, compound eyes are highly sensitive to moving objects [42].

Influenced by the living environment, the function of amphibious imaging is critical for creatures that live in both air (refractive index ~ 1.0) and water (refractive index ~ 1.33). Amphibians have evolved unique eye structures to adapt to environments with different refractive indices, such as flat corneas (fiddler crabs) and complex focusing systems (diving ducks) [43, 44].

2.3 Nervous system for data processing

The human visual system consists of the eye, the eye appendages, the visual pathways, and the visual center in the brain. The retina of the eye is covered with a large number of nerve cells and its simplified structure is shown in Fig. 1d. The retina is organized into three nuclear layers (outer nuclear layer (ONL), inner nuclear layer (INL), ganglion cell layer (GCL)) and two synaptic layers (outer plexiform layer (OPL), inner plexiform layer (IPL)). Light travels in the opposite direction to the information in the retina. Specifically, light entering the eye travels through the tissues and reaches the ONL at the base of the retina. The ONL is made up of photoreceptors, including cones and rods, which convert light signals into electrical signals. In the OPL, the electrical signals are then received by at least 13 types of bipolar cells after being collated by horizontal cells. Different types of bipolar cells collect specific signals and systematically transform them to further process the information in the retina. And bipolar cells are the only nerve cells that connect the OPL and IPL. The IPL contains bipolar cells, amacrine cells, and ganglion cells (RGCs). Amacrine cells can provide inhibitory or neuromodulatory inputs to bipolar cells and RGCs. When the electrical signal reaches the IPL, it is collated and encoded by the RGCs as a series of spikes with complex patterns and transmitted through the optic nerve to higher visual centers, ultimately forming a vision in the visual cortex region of the brain [45]. Notably, the process of transmitting signals between neurons across synapses induces synaptic plasticity, which plays a key role in the effectiveness of signal processing [46, 47].

3 Bio-inspired curved vision systems

Using the curved retina, biological eyes can achieve complex and precise imaging in a small space. In addition, biological eyes perform a variety of functions to ensure the survival and reproduction of living organisms. The development of the visual system is moving towards miniaturization and integration. However, it has reached a bottleneck due to the limitations of the planar image sensor. In recent years, biomimetic technology has made significant contributions to the progress of science and technology by drawing inspiration from the structures and functions of biology [48–55]. Applying the curved imaging structure of biological eyes to the camera solves the miniaturization problem while inheriting the unique functions of biological eyes, such as wide field of view, adjustable focus, deep depth of field, dynamic imaging, wide spectral response, amphibious imaging, and so on. A comparison of curved vision systems with different functions and characteristics is summarized in Table 1 [56–71].

3.1 Wide field of view

To capture as much visual information as possible, chambered eyes have a wide field of view. The curved retina directly compensates for the aberrations of the curved focal plane. Thus, the human eye with a compact structure can achieve a wide field of view (~ 120°) [72] (Fig. 2a). However, limited by the planar image sensors, the field of view of conventional commercial cameras is small. The number of lenses must be increased to achieve wide-angle imaging. This results in a huge volume and high cost [73, 74]. To mimic the human retina, Gu et al. [61] demonstrated hemispherical curved surface imaging through in situ prepared perovskite materials (Fig. 2b). In detail, high-density formamidinium (FA) lead triiodide ($FAPbI_3$) perovskite nanowire arrays were grown in a hemispherical porous aluminum oxide membrane (PAM) by vapor deposition to obtain the curved image sensor in one step. Figure 2c shows the scanning electron microscope (SEM) image of the nanowire arrays with a pitch of 500 nm and a density of 4.6×10^8 cm^{-2}. The resolution was much higher than that of the human retina. The tungsten film and glassy ionic liquid on the hemispherical aluminum shell were used as co-electrodes, and the flexible eutectic gallium indium liquid wire was used as the counter electrode. A 10×10 curved surface image sensor array was fabricated. Then the curved image sensor was assembled with the corresponding lens to form a spherical bionic electrochemical eye (EC-EYE). Figure 2d shows that the spherical EC-EYE had a diagonal field of view of ~ 100.1°, which was obviously better than that of a flat device (69.8°). Besides the human eye, many other chambered eyes also have a wide field of view, which are extensively used in wide field of view (FOV) imaging [75, 76].

For biological eyes, spherical aberration affects the field of view at large apertures. Spherical aberration is the only monochromatic aberration of a point on an axis. It can be defined as the change in image distance or focal length with the aperture in the case of infinite conjugation. Specifically, for parallel incident light, rays at different distances from the optical axis intersect at different points on the axis [77]. Biological eyes have two solutions to adjust the spherical aberration. One is to make the outer region of the refractive surface flat relative to the center. The other is to make the

Table 1 Summary of characteristics and functions of curved vision systems (ZM: zooming mode)

Curved structure	Material	Pixel number*	Fabrication strategy	Function	Refs.
Curved image sensor	Si	23 × 23	Island-bridge	FOV: 120°; ZM: change in distance of sensor; DOF: 20 cm to infinity; wavelength: 850 nm	[56]
		180	Island-bridge	FOV: 160°; DOF: infinity; wavelength: 532 nm	[57]
		256	Ultrathin design	FOV: 300°(H) 160°(V); DOF: infinity; amphibious Imaging	[58]
		281	Origami	FOV: > 72°; wavelength: 543, 594, 633 nm	[59]
		32 × 32	Kirigami	ZM: electrically tunable lens and change in curvature of sensor	[60]
	Perovskite ($FAPbI_3$)	10 × 10	In situ growth	FOV: 101°	[61]
	Graphene/MoS_2/Graphene	7 × 8	Ultrathin design	Wavelength: 405, 532, 685, 785, 904 nm	[62]
	DPPT-TT: N2200	9 × 10	Ultrathin design	Wavelength: 808 nm	[63]
	Perovskite ($PEA_2FA_3Pb_4X_{13}$)	–	In situ growth	FOV: 180°; wavelength: 550, 600, 660, 820 nm	[64]
	isQDSN	5 × 5 × 3	Intrinsic stretchability	Wavelength: 450, 525, 630 nm	[65]
	$CsPbI_3$	–	In situ growth	FOV: 140°; ZM: change in focal length of artificial crystalline lens; wavelength: 405, 520, 650 nm	[66]
Microlens arrays	CCD	–	–	FOV: 180°; ZM: tunable optofluidic chamber; DOF: infinity	[67]
	CMOS	–	–	FOV: 68°	[68]
		4400	–	FOV: 122.4°; DOF: infinity	[69]
		522	–	FOV: 170°; DOF: infinity; dynamic imaging	[70]
		19	–	FOV: 90°; DOF: infinity; dynamic imaging	[71]

*For curved surface sensor, data is the number of pixels; for microlens arrays, data is the number of lenses

lens have an appropriate refractive index gradient [4]. Fish eyes have spherical lenses, whose central refractive index is higher than that of the outer gradient lens. This causes light rays further from the axis to bend less, reducing spherical aberration [78, 79]. The spherically symmetric lens and hemispherical retina of the fish allow for a much wider field of view (~ 160°) than the human eye with a single optical axis [38] (Fig. 2e).

Inspired by the aquatic eye, Kim et al. [56] demonstrated a bioinspired camera with a wide field of view by mimicking the structure of fish eyes (Fig. 2f). To mimic the fish lens with a gradient refractive index, the monocentric spherical lens adopted a core–shell structure. The refractive index (n_{in} = 1.52) of the inner core (BK7) was smaller than that of the outer shell (SF16, n_{out} = 1.65). Figure 2g summarizes the characteristics of wide-angle multi-lens, homogeneous spherical lens, and monocentric lens, including spherical aberration (SPHA), coma, astigmatism (ASTI), chromatic transversal aberration (CTA), and chromatic longitudinal aberration (CLA), showing the excellent optical performance of the gradient spherical lens. And a network of 23 × 23 hexagonal silicon photodetector arrays (h-SiNR-PDA) was fabricated on a plane, perfectly mimicking the hemispherical retina of fish. Then, the aquatic vision-inspired camera module was obtained by integrating the gradient spherical lens with h-SiNR PDA. Figure 2h quantitatively validates the aberration-free wide-FOV imaging for the bioinspired camera. The cross pattern from − 60° to 60°, every 15° a point (Fig. 2h, illustration) was imaged on an h-SiNR PDA. It could be seen that each point could be clearly imaged without distortion, showing a FOV of 120°. Furthermore, the FOV of bioinspired cameras could be further improved to 160° by using advanced lens manufacturing methods and a larger array of image sensors.

The male Xenos peckii has an unusual eye structure of each ommatidium consisting of a large lens and several photoreceptors. Compared to the ommatidia of the apposition compound eye, it has only one or a few photoreceptors, providing higher resolution [80–82]. In this case, the ommatidia of male Xenos peckii can be seen as a kind of chambered eye. Inspired by the structure of male Xenos

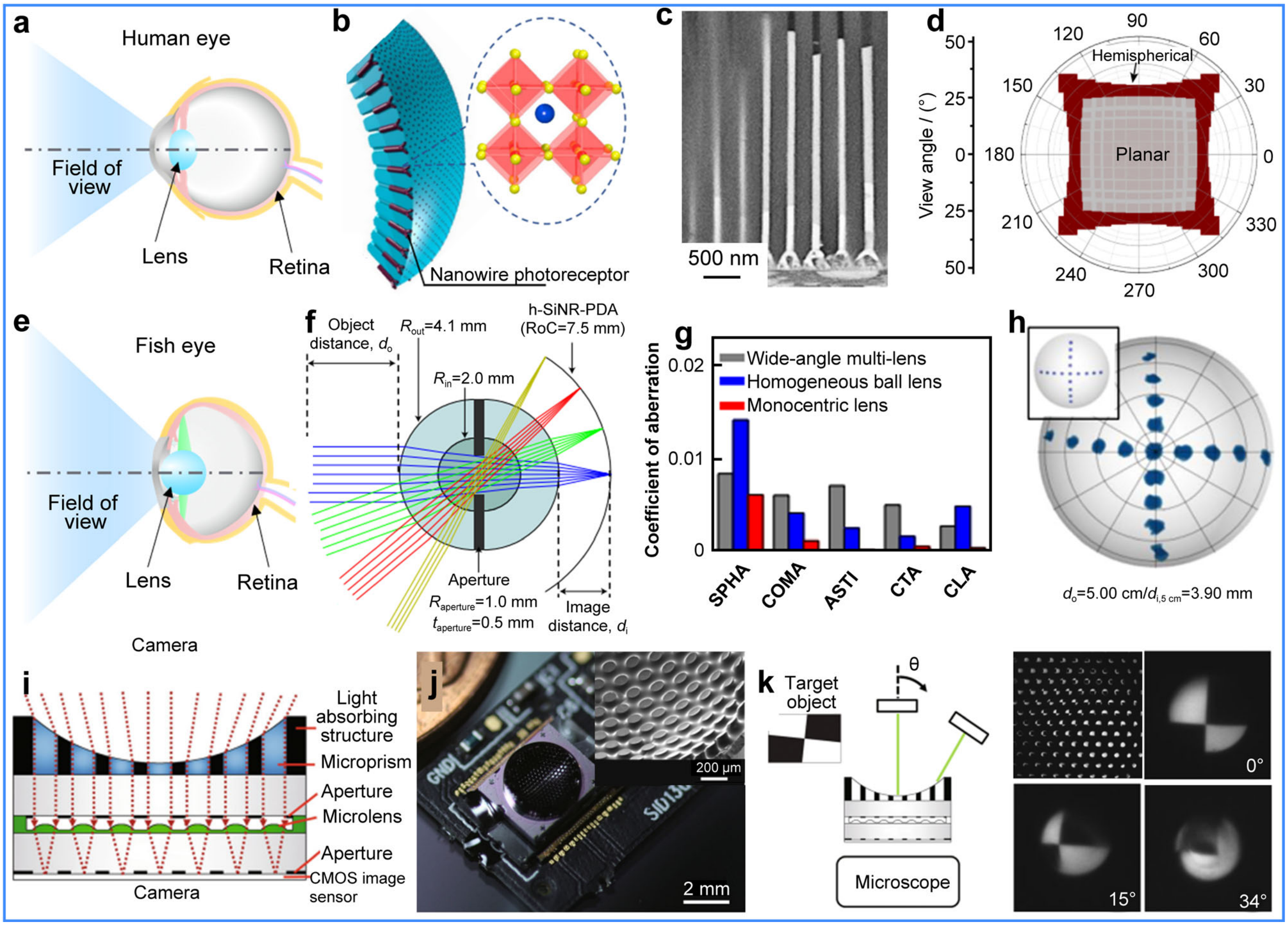

Fig. 2 **a** Schematic illustration of wide field of view of human eyes; **b** schematic diagram and **c** cross-sectional SEM image of perovskite nanowires grown in-situ in a hemispherical PAM template; **d** FOV of planar and hemispherical imaging systems. Reproduced with permission from Ref. [61]. Copyright 2020, Nature Publishing Group. **e** Schematic illustration of wide field of view of fish eyes; **f** structure of aquatic inspired camera; **g** Seidel aberration coefficients of wide-angle multi-lens, homogeneous ball lens, and monocentric lens; **h** quantitative test results of FOV imaging with a cross pattern composed of spots and (inset) original image of cross spot. Reproduced with permission from Ref. [56]. Copyright 2020, Nature Publishing Group. **i** Schematic illustration of structure of Xenos Peckii-inspired camera; **j** optical image of bioinspired camera and (inset) SEM images of concave microprism arrays after filling with black polymer; **k** schematic diagram of experimental setup for FOV testing and images at three different angles of incidence. Reproduced with permission from Ref. [68]. Copyright 2018, Nature Publishing Group

peckii eyes, Keum et al. [68] developed a biologically inspired ultrathin digital camera. The specific structure was shown in Fig. 2i. The top layer contained microprism arrays with titled optical axes, between which was the light-absorbing structure. The middle layer consisted of hexagonal microlens arrays focusing the light from the microprism and a Cr barrier layer blocking the light from adjacent channels. The bottom layer was the planar CMOS image sensor and a light barrier layer to reduce optical crosstalk. Particularly, the microprism arrays with tilted optical axis could change the angle of view to obtain a large field of view. Figure 2j shows the photograph of the bioinspired camera with a diameter of 3.4 mm. The inset in Fig. 2j was a SEM image of the microprism arrays with a diameter of 100 μm and a pitch of 80 μm. In Fig. 2k the FOV of the concave imaging structure was tested. By changing the angle between the target object and the main optical axis, corresponding images of different channels were acquired from three different angles of incidence. And when the angle of incidence was 34°, the target image could still be obtained, indicating that the FOV was 68°.

Unlike concave chamber eyes, each ommatidium in compound eyes is a separate imaging unit. The ommatidia have their optical axes and are integrated to form a convex hemisphere. This allows light from different directions to meet a matching optical axis. As a result, the apposition compound eye has an extremely wide field of view [39] (Fig. 3a). Therefore, convex compound eye structures have been extensively studied in wide FOV imaging [57–59, 64, 67, 69–71, 83]. With reference to the compound eye structure of arthropods, Song et al. [57] demonstrated a bioinspired vision system with an almost completely hemispherical geometry. The structure of the imaging system could be mainly divided into two parts (Fig. 3b). One was a 16 × 16 microlens array made of elastic polydimethylsiloxane (PDMS) (refractive index ∼ 1.43). Each microlens had a radius of curvature of about 400 µm, and it was mounted on a cylindrical column about 400 µm high, which played the role of strain isolation. All the microlenses were connected by a base membrane about 500 µm thick. The other part was an array of silicon photodiodes with serpentine interconnections. The serpentine interconnection was the typical island-bridge structure, a common way to make rigid devices stretchable [84–87]. The photodiode arrays were integrated at the focal points of the microlens arrays by alignment bonding. The bionic compound eye structure was then formed. Based on the good elasticity of the PDMS and the deformability of the photodetectors given by the island-bridge structure, the hydraulic actuation could transform the integrated device from a planar structure to a hemispherical structure (hemisphere radius of curvature of R ∼ 6.96 mm). After deformation, micro X-ray computed tomography (XCT, MicroXCT 400) and finite element method (FEM) calculations were used to analyze the structure of the device. The results showed that the combination of microlens and column had a greater thickness than that of the base film, reducing the strain at the bond with the photodetector and showing good isolation. As a result, the device was not dislocated, electrically damaged, or optically altered during the deformation process. Because the hemispherical compound eye structure had a wide field of view without off-

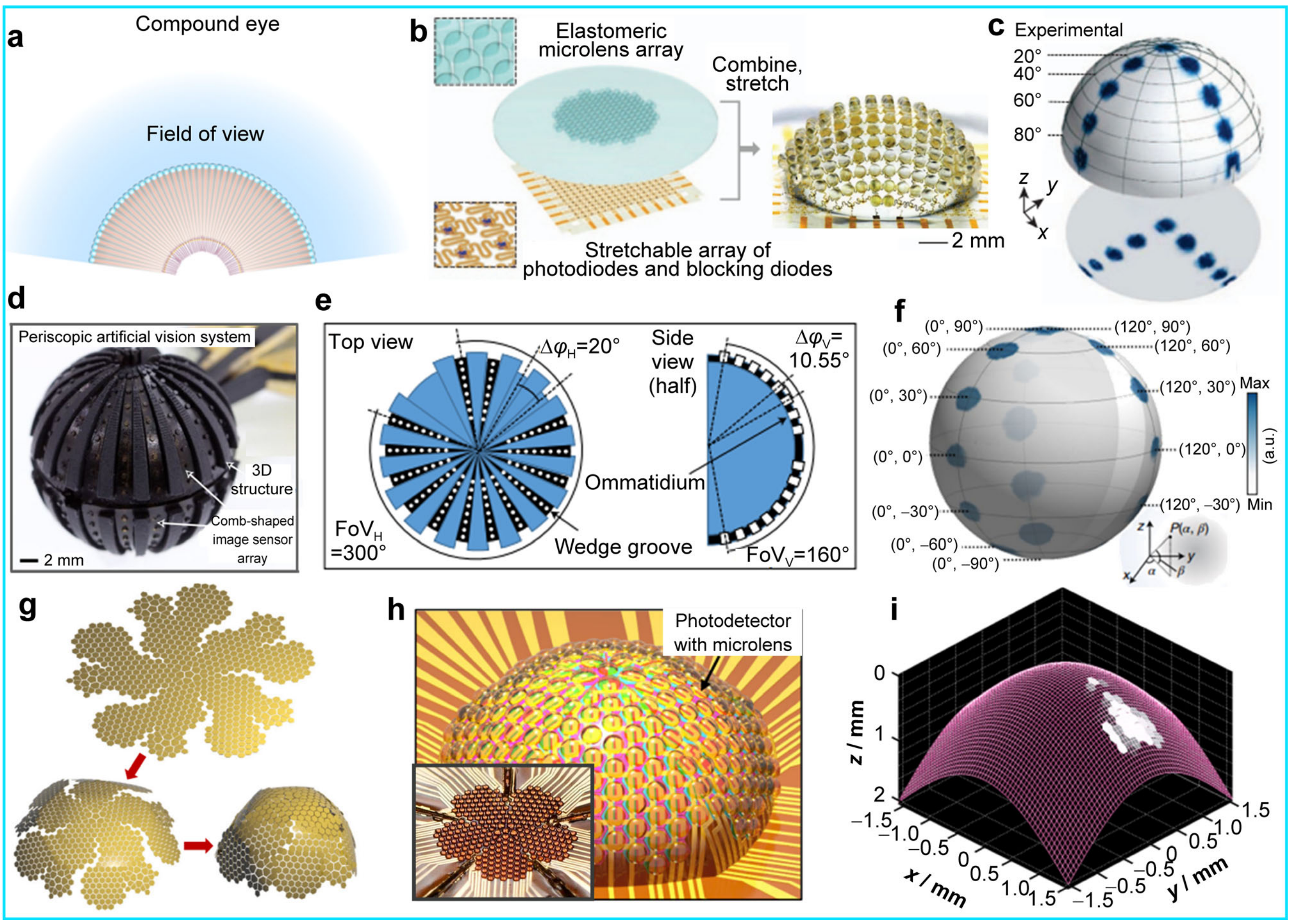

Fig. 3 **a** Schematic illustration of wide field of view of compound eyes; **b** combining an elastomeric microlens array (above) and a photodetector array (below) to form a curved apposition compound eye camera (right) through elastic deformation; **c** quantitative test results of FOV imaging with a collimated laser beam at nine different angles of incidence. Reproduced with permission from Ref. [57]. Copyright 2013, Nature Publishing Group. **d** Optical image of artificial vision system; **e** top view (left) and side view (right) of pixel distribution on 3D structure; **f** imaging results of FOV with three sequential illuminations of six collimated laser beams. Reproduced with permission from Ref. [58]. Copyright 2022, Nature Publishing Group. **g** Schematic illustration of a folding polygon block made up of pentagons and hexagons into a hemisphere; **h** schematic illustration of convex hemispherical artificial camera based on origami structure and (inset) optical figure of planar device; **i** image of laser spot obtained from convex artificial camera. Reproduced with permission from Ref. [59]. Copyright 2017, Nature Publishing Group

axis aberration. The FOV of the hemispherical bionic eye was quantitatively analyzed in Fig. 3c. When the laser was irradiated from − 80° to 80° with a step of 20°, the image pattern was clear with relatively uniform size and shape. The total field of view was ~ 160°. And it was consistent with the predicted results.

Furthermore, the ommatidia of fiddler crabs cover almost the entire eye stalk, giving them an almost panoramic view. Inspired by this, Lee et al. [58] fabricated the spherical artificial vision system with a panoramic visual field. As shown in Fig. 3d, the surface of the artificial vision system was almost full of artificial ommatidia. Each pixel consisted of an ultrathin image sensor and a microlens. Flexible polyurethane (PU) seals were inserted in the center to act as strain isolation. Eight pixels were assembled to form a comb-like sensor unit. Since Young's modulus of the microlens array was greater than that of the PU gasket, the stress on the microlens array after bending was negligible. Owing to the flexibility of the ultrathin structure, the photodetector arrays could maintain stable performance when assembled. Based on this, four comb-like units were assembled on a spherical structure with grooves to obtain a panoramic vision system. The specific structure was shown in Fig. 3e. In the top view (Fig. 3e), the included angle of adjacent grooves was 20°, and the horizontal field of view covered 300° except for the empty area. In the side view (Fig. 3e), the included angle of adjacent sensors was 10.55°, and the vertical field of view covered 160°. The FOV of the device was then quantitatively analyzed by laser spot irradiation at different angles. Figure 3f shows that imaging could be performed in the entire field of view except for the blind spot of the data readout port.

In geometry, convex isogonal polyhedra allow certain polygon combinations to be folded into spheres. Thus, origami structure is another method to obtain the curved image sensor [59, 76, 88–90]. Zhang et al. [59] used the origami structure to fabricate hemispherical artificial compound eyes. Figure 3g is the schematic illustration of the method. Truncated dodecahedrons were divided into 676 polygons, so a hemisphere could be obtained by folding and joining this structure. The photodetector arrays were fabricated on the planar flexible substrate using planar processing technology and then trimmed to obtain the polygonal structure. By folding the structure upwards, hemispherical arrays could be obtained, which could be used for retina-like imaging. And the convex array could be achieved by folding the device downwards. It could be used to simulate compound eyes. In the artificial compound eye vision system, the lens arrays were fabricated in situ on each photodetector by a photoresist reflow method (Fig. 3h). To verify the wide field of view of the artificial compound eye, a laser beam was illuminated at 36° from the horizontal plane and the corresponding image pattern was obtained (Fig. 3i). Because the lens structure of the device without the anti-optical crosstalk structure was relatively simple, the imaging pattern was blurred rather than one with a clear outline. However, it still demonstrated the characteristics of a wide FOV of the compound eye structure.

The wide field of view of bioinspired eyes has been extensively studied and can be categorized into two types: the chambered eye and the compound eye. The chambered eye employs a concave image sensor, which can block some of the incoming light and thus makes it difficult to achieve a full 360° panoramic view. Moreover, the curved image sensor requires careful adaptation to the lens for imaging. Due to the optical principle of the lens, the off-axis difference in the wide field of view can cause image distortion, making it challenging to further improve the field of view. In contrast, the compound eye uses a convex image sensor that does not block incoming light and can receive light from all directions, facilitating panoramic imaging. The optical structure of the compound eye comprises an array of lenses that divide the field of view, with each lens only needing to focus on a small area of light. As a result, the compound eye overcomes many of the optical limitations of the chambered eye, making it the preferred choice for achieving a wider field of view.

3.2 Adjustable focus

A majority of chambered eyes have optical light management components that adjust the focal length to see objects at different distances. The lens of the human eye is an important part of the refractive system of the eyeball, and it is also the only interstitial body that can regulate refraction. By contracting or relaxing the ciliary muscle, the diopter can be altered with the changes in the curvature of the lens, which allows the light to be focused precisely on the retina when looking up close or at a distance [23] (Fig. 4a). Inspired by this property, Rao et al. [60] proposed a shape-adaptive image sensor based on a kirigami structure coupled with an electrically tunable lens to achieve clear imaging of objects at different distances. The kirigami structure was made by cutting the non-stretchable whole into interconnected small units, and the small units could rotate when stretched, making the structure deformable [91–94]. Figure 4b is a schematic illustration of the device with a kirigami structure and its constructed convex imager. This structure had a high pixel fill factor (~ 78%), much higher than other reports. Thus, the kirigami structure was well suited to simulate a high-resolution retina. Biaxial strains with different levels were applied to the device and the corresponding strain distributions were simulated (Fig. 4c). The results showed that the strain was concentrated at the corners and hinges. The active device with the square pixel had the smallest internal strain,

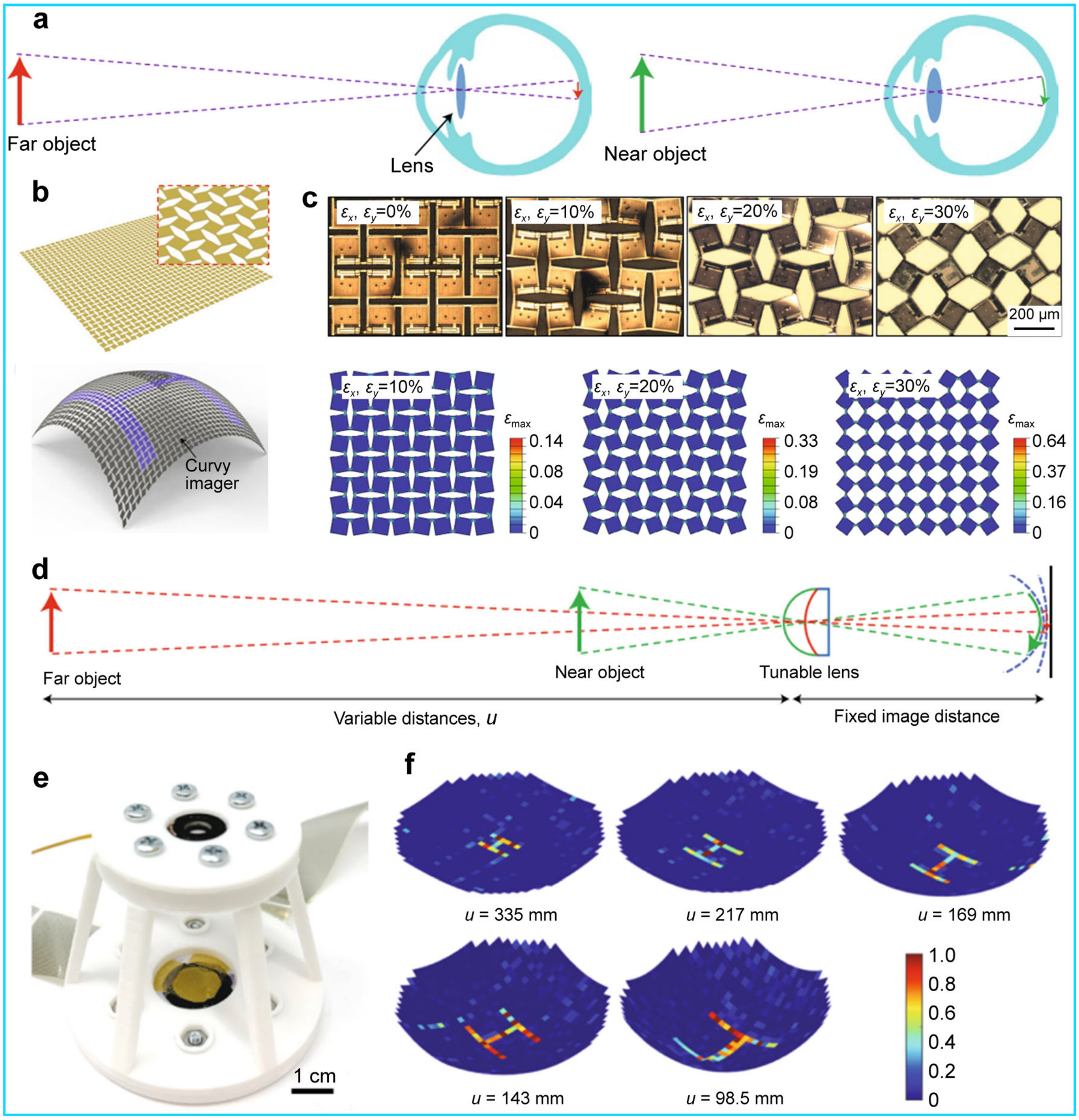

Fig. 4 **a** Schematic illustration of human eye adjusting its focal length by changing shape of lens; **b** schematic illustration of a kirigami sheet biaxial stretching (above) and bending into a convex image sensor (below) and (inset) enlarged structure; **c** optical images (above) and simulated strain profiles (below) of kirigami image sensor at different biaxial tensile levels; **d** schematic illustration of zoom principle of imaging system with adaptive imager and tunable focusing power; **e** optical image of artificial camera with adaptive imager; **f** imaging results obtained by an adaptive imager when objects are located at different distances. Reproduced with permission from Ref. [60]. Copyright 2021, Nature Publishing Group

ensuring the mechanical stability of the device during deformation. Figure 4d shows the imitation principle of the adjustable focusing function. Specifically, the electrically tunable lens and the concave imager were assembled with the fixed distance (Fig. 4e). The images at different object distances could be obtained by changing the focal length of the lens and the curvature of the adaptive imager. To achieve the curvature adjustability of the imager, conformal additive stamp (CAS) printing technology was used to transfer a planar imager onto a concave magnetic rubber composite. The curvature of the imager could be changed by applying an external magnetic field. And the focal length of the electrically tunable lens could be adjusted by changing the applied current. Images of objects at different distances could then be obtained (Fig. 4f). As the object distance decreased, the radius of the electrically tunable lens and the imager increased. Although the size of the image changed, the imaging focusing effect remained well.

And it was significantly better than that of the plane imager. The imaging results confirmed that the artificial eye achieved the effect of human-like zoom.

Unlike land vertebrates, fish has an almost incompressible spherical lens. Therefore, the method of zooming by adjusting the curvature of the lens is not suitable for fish. Instead, they move the lens to change the focal length. When the object is far away, the lens of fish is usually close to the nasal pole of the eye. When the object is close, the lens moves away from the nose along the eccentric axis of the pupil [4] (Fig. 5a). For example, when the object distance (d_o) was 10 cm, the imaging distance (d_i) was 3.55 mm. When the d_o was less than 10 cm, the focal length became longer than 3.55 mm, so it was necessary to change the d_i to focus the images on the retina. Kim et al. [56] fabricated an artificial imaging system by integrating a monocentric lens and a hemispherical image sensor to realize the visual function of aquatic animals. To mimic the hemispherical retina of fish, h-SiNR-PDA with the island-bridge structure was fabricated. The serpentine interconnections and ultrathin thickness made them deformable. The finite element analysis (FEA) showed that the strain was mainly concentrated in the interconnection area (Fig. 5b). And the strain of the sensor part was 0.02%, much smaller than the fracture strain of silicon ($\sim$ 1%). No mechanical fracture or device failure occured when the device was transferred to the concave hemispherical structure (Fig. 5c). The hemispherical sensor was then combined with a gradient index lens to create a bioinspired camera with the ability to adjust the focal length. In Fig. 5d, the objects with $d_o = 10$ cm could be clearly imaged at $d_i = 2.95$ mm, but if d_o was less than 10 cm (e.g., $d_o = 3$ cm) the image was blurred (Fig. 5d). A clear image was obtained by moving imager to change d_i for refocus (Fig. 5d).

In comparison to chambered eyes, insect compound eyes cannot change their focal length. Their eyes have a deep depth of field and can theoretically see objects at infinite distances. But it's difficult for them to judge distances. Combining the characteristics of chambered eyes to create compound eyes with adjustable focus can solve this problem [95–97]. Cao et al. [67] introduced the adjustable-focus lens into the artificial compound eyes and realized distance recognition by zoom imaging. The structure of the device was shown in Fig. 5e. The deformable PDMS microlens array was fabricated by femtosecond laser processing, wet etching, and soft lithography. The microlens array was then assembled onto the microfluidic chamber. By controlling the amount of solution injected into the chamber, the focal length of the artificial compound eye could be adjusted to achieve dynamic zoom. Figure 5f shows the relationship between the focal length of the main lens and the volume of the chamber. As the volume of the chamber increased, the focal length decreased from 4.73 to 3.03 mm. The zoom imaging capability of the instrument was further verified. The test apparatus was shown in Fig. 5g. Two imaging masks with "S" arrays and "K" arrays were located at 1183 and 1165 μm, respectively. As the solution was injected into the chamber, the focal length of the artificial compound eyes gradually decreased. Initially, only a blurred spot could be seen (Fig. 5h). As the focal length gradually decreased, the pattern of the distant letter "K" became clearer. However, as the focal length was further reduced, the pattern of the letter "K" became blurred and the pattern of the letter "S" became clear. All of this confirmed that the device was capable of zoom imaging.

3.3 Deep depth of field

Unlike the human eye, insects cannot dynamically change the focus of compound eyes. To obtain clear images of objects at different distances, insects have evolved an imaging system with a deep depth of field. Depth of field in object space is defined as the range of distances in which the object can produce a sharp image on the retina. In geometrical optics, the depth of field of an optical system can be characterized by the object distance (L), focal length (f), pupil size (D), and maximum spot diameter (B) [98]:

$$\mathrm{DOF} = \frac{2L^2 fDB}{(fD)^2 - (LB)^2} \tag{1}$$

where the object distance L and the maximum spot diameter B are held constant, a smaller focal length f and pupil size D lead to a deeper depth of field. Ommatidia of insects have a much smaller size (ranging from 10 to 140 μm in diameter) and lens focal length than those of human eyes. Therefore, the small lens of the ommatidia give the insect a deep depth of field. Alternatively, the resolution is another factor limiting the depth of field [99]. The resolution of insects is very low, usually a few thousand. As a result, the images the insects see are mosaics [100]. Fortunately, this sacrifice in resolution gives insects a deep depth of field, which allows insects to simultaneously image objects at different distances.

Similarly, deep depth of field is very important for artificial vision systems and has great potential for applications such as surveillance devices, endoscopy tools, [101–103]. Inspired by the compound eyes of insects, Song et al. [57] used deformable photodetector arrays and microlens arrays to fabricate a 180-pixel hemispherical artificial compound eye system. For the quantitative characterization of the depth of field of artificial compound eyes, imaging tests were performed using the experimental apparatus as shown in Fig. 6a. Concretely, the triangular and circular objects were placed at different angles of the

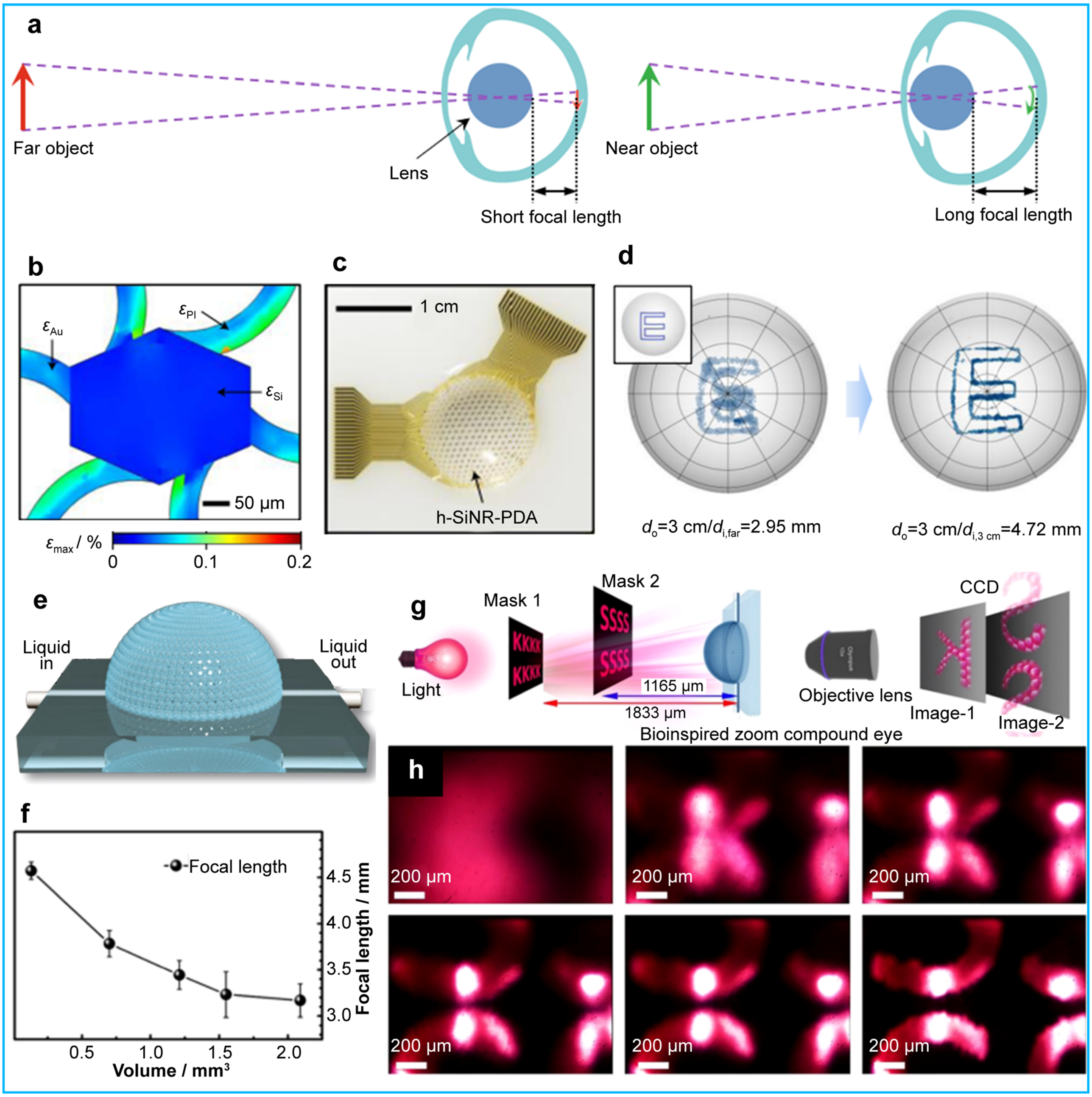

Fig. 5 **a** Schematic illustration of aquatic eye adjusting its focal length by moving protruding monocentric lens; **b** finite element analysis of strain distribution in hexagon pixel of h-SiNR-PDA; **c** optical image of hemispherical SiNR photodiode array; **d** bioinspired camera zoom demonstration (d_o = 3 cm), where image captured with $d_{i,far}$ = 2.95 mm is blurry (left), but it can be refocused with $d_{i,3\ cm}$ = 4.72 mm (right), and (inset) image of original object. Reproduced with permission from Ref. [56]. Copyright 2020, Nature Publishing Group. **e** Schematic illustration of variable-focus compound eye; **f** relationship between focal length and chamber volume of main lens; **g** schematic illustration of experimental setup for zoom imaging with masks "K" and "S" at different positions; **h** images captured by bioinspired zoom compound eyes as volume of cavity increases. Reproduced with permission from Ref. [67]. Copyright 2020, American Chemical Society

artificial compound eye. The position of the triangular object was fixed (D_A = 12 mm), while the position of the circular object was varied (D_B = 12, 22, 32 mm), and then three imaging patterns were obtained (Fig. 6b). The results showed that no matter where the object was located, it could be focused to obtain a clear image. However, the size of the image pattern varied. The further away the object was, the smaller the image pattern was.

Shi et al. [69] took a different approach to create a hemispherical compound eye camera system (SCECam).

The SCECam could be divided into three parts: a hemispherical compound eye, an optical relay system, and a CMOS planar imaging sensor (Fig. 6c). The hemispherical compound eye integrated ~ 4400 microlenses on a curved surface. It was obtained by preparing the microlens array on a plane and then transferring it to a hemispherical glass dome by thermal pressing. Combining directly the curved microlens array with a planar image sensor is a common method to achieve an artificial compound eye system [83, 104–110]. Nevertheless, Shi et al. [69] made improvements on this basis by introducing an optical relay system between the hemispherical compound eye structure and the planar sensor. The optical relay system could transform the curved focal plane into a plane, thus solving the problems of field curvature, vignetting, and distortion of the camera system. Simultaneously, the SCECam reserved the basic characteristics of the compound eye, such as a wide field of view and deep depth of field. Compared to the traditional compound eye system, SCECam had better image quality. In Fig. 6d, although the pentagon pattern was at different distances (D = 20, 40 and 80 mm), it could be well-focused due to the deep depth of field. Of course, the size of the pattern was affected by the distance, but the sharpness of the image was not greatly

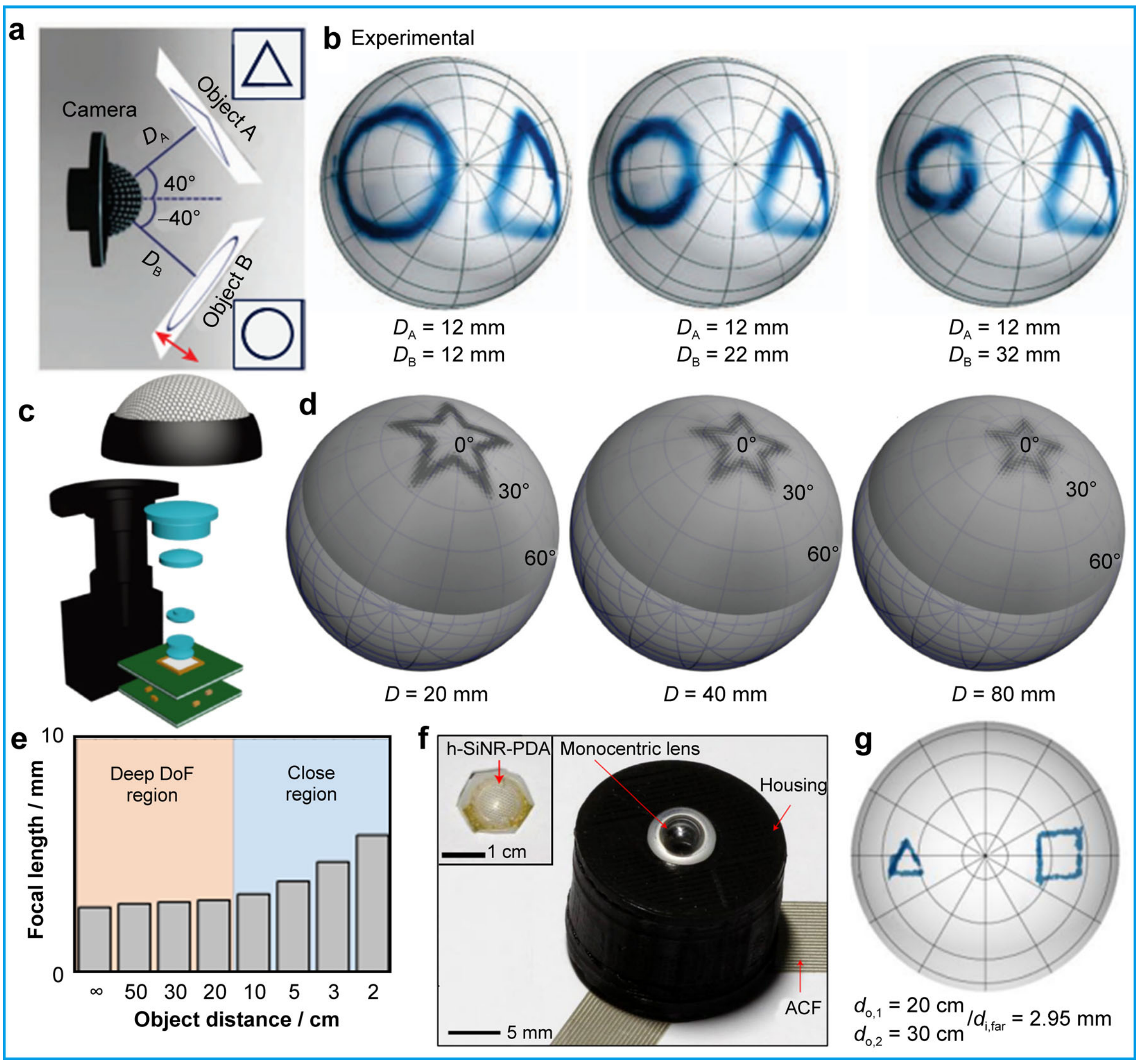

Fig. 6 **a** Schematic illustration of an experimental setup to demonstrate DOF, where Object A (triangle) lies at an angular position of 40°and distance D_A; Object B (circle) at − 40° and D_B; **b** images obtained at different values of D_B. Reproduced with permission from Ref. [57]. Copyright 2013, Nature Publishing Group. **c** Schematic diagram of structure of SCECam; **d** images captured by SCECam with objects located at different distances. Reproduced with permission from Ref. [69]. Copyright 2017, Optical Society of America. **e** Focal lengths for objects at various distances, focused by monocentric lens; **f** optical photo of bioinspired camera and (inset) h-SiNR-PDA; **g** imaging demonstration for a triangle (Object 1) and square (Object 2) located at different distances ($d_{o,1}$ = 20 cm and $d_{o,2}$ = 30 cm) and at different angles with a 90° difference, where image is captured with $d_{i,far}$ = 2.95 mm. Reproduced with permission from Ref. [56]. Copyright 2020, Nature Publishing Group

affected, showing the advantage of the deep depth of field of the compound eye.

Besides insects, fish with a short focal length also has a deep depth of field [111]. Inspired by the aquatic vision, Kim et al. [56] prepared a bioinspired camera consisting of a monocentric lens and a hemispherical photodetector array. With a focal length of only 2.79–5.87 mm, the monocentric lens could produce a deep depth of field. The concrete imaging principle was shown in Fig. 6e. When the distance between the object and the lens exceeded 20 cm, the focal length was essentially the same at around 2.95 mm. This meant that clear imaging could be achieved as long as the imaging distance was fixed at 2.95 mm. However, if the object distance was less than 20 cm, the focusing distance would change significantly. The monocentric lens was assembled with a hemispherical h-SiNR PDA image sensor to create a bioinspired camera and its deep depth of field was verified (Fig. 6f). More specifically, the triangular object was placed 20 cm away from the bionic camera, while the object distance of the square object was 30 cm. According to the above imaging principle, the image distance needed to be only 2.95 mm for clear imaging. The imaging results showed that the triangle and square patterns were clear and there was no blurred situation due to different object distances, as shown in Fig. 6g. This confirmed that the artificial vision system inspired by aquatic vision had a deep depth of field.

3.4 Dynamic imaging

The basic life activities of insects, such as target recognition and tracking, highly aerobatic flight maneuvers, obstacle avoidance, and soft landing on objects, are inseparable from dynamic imaging. Insects have excellent dynamic vision thanks to their compound eyes. As each ommatidium in the compound eye can only receive light along its optical axis, the intensity of the light received by each ommatidium changes significantly when the detection target moves. This phenomenon is called the flicker effect, and the rate of opening and closing is called the flicker frequency. The compound eye has a high flicker frequency, which allows it to process image information faster than the chambered eye. This unique effect makes insects highly sensitive to moving objects in their field of vision. For example, honeybees were reported to respond to an object appearing in their field of view within 0.01 s, while humans took five times longer [42].

The artificial compound eyes with excellent dynamic imaging capability have been used to realize three-dimensional (3D) point position recognition and target tracking [70, 71, 112–114]. Following the structure of apposition compound eyes, Dai et al. [70] fabricated the biomimetic apposition compound eye (BAC-eye) through a microfluidic-assisted 3D printing technique. The structure of the device was shown in Fig. 7a. Briefly, the BAC-eye consisted of 522 microlenses, cylindrical posts, waveguides transmitting light to the planar base, and a hemispherical mold with hollow tubes corresponding to the lenses, crystalline cones, rhabdoms and pigment cells of compound eyes. SEM image of the BAC eye (Fig. 7b) showed that the microlenses were evenly distributed on the hemispherical dome, giving it a wide field of view of 170°. Ray tracing of the structure confirmed that light could be well confined within the ommatidia and transmitted to the bottom plane. Therefore, it could be combined with any planar image sensor to create a curved vision system. To demonstrate the dynamic imaging capability of the BAC eye, the 3D point source tracking experiment was adopted. By illuminating the green optical fiber on the BAC-eye, corresponding light spots could be obtained on the CMOS camera. According to the size and central position of the spot, the 3D position of the optical fiber could be tracked. Figure 7c shows 3D positioning of the optical fiber. First, the optical fibers were measured at different positions and the device was calibrated to obtain the calibration curve between spot distance and spot width (Fig. 7d). Then the positions of the optical fibers were determined. As demonstrated in Fig. 7c, the yellow circle and the green circle were the actual positions and the measured position, respectively, which were in good agreement. Thus, the BAC-eye was verified having excellent 3D position tracking ability and could be applied to navigation and search fields.

Currently, most bioinspired compound eyes use simple spherical lenses with poor optical performance, resulting in image defocus. As a solution, Hu et al. [71] presented a photoelectric integrated μ-compound eye (μ-CE) camera with logarithmic ommatidia by femtosecond laser two-photon polymerization. Due to the logarithmic ommatidia, the μ-CE camera had a deeper depth of field and a larger focusing range than those of the bioinspired compound eyes with simple spherical lenses. And the μ-CE camera could detect the trajectory of moving objects. Figure 7e displays the method to record the trajectory of the beetle's movement in real time. Figure 7f, g shows the images of the beetle taken by a conventional digital camera and the μ-CE camera at different time. According to the sharpness of the images taken by the different ommatidia, the distance and direction angle of the beetle could be obtained which allowed the beetle's trajectory to be reconstructed. The corresponding reconstruction principle was schematically illustrated in Fig. 7h. In detail, the μ-CE camera could obtain images of the target object with different sizes and positions from different ommatidia. Based on this set of images, the spatial position of the target object could be reconstructed. The bioinspired camera was used to detect the activity of green paramecium in the reservoir to

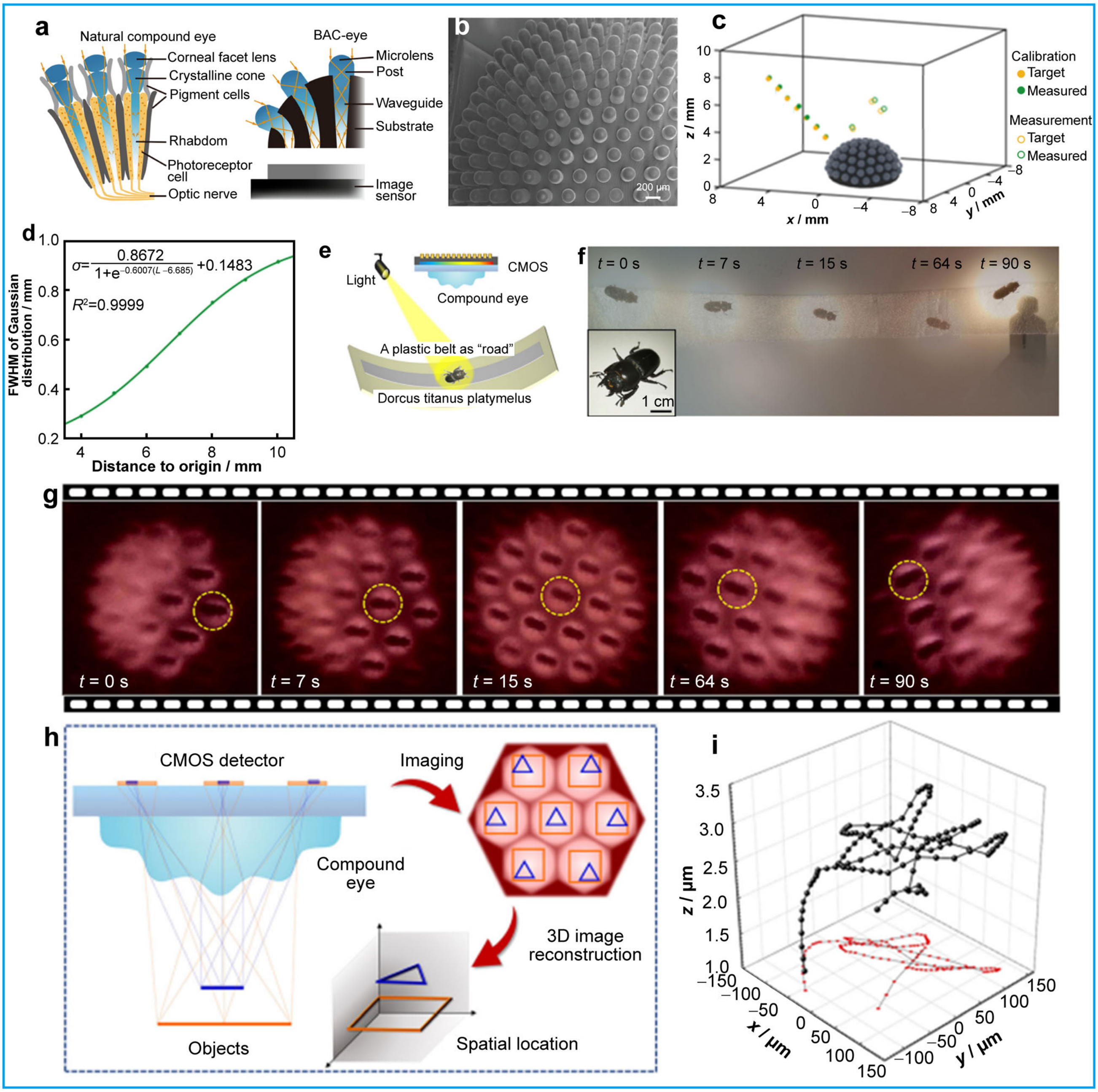

Fig. 7 **a** Structural diagram of arthropod compound eye (left) and cross-section of BAC-eye (right); **b** SEM image of a BAC-eye; **c** experimental results for tracking location of light sources by BAC-eye, where solid dots are target and measured positions used for calibration, respectively, and yellow and green circles are target and measured positions with unknown light locations; **d** dependence of FWHM of light distribution captured by BAC-eye with respect to distance from original point to light spot. Reproduced with permission from Ref. [70]. Copyright 2021, Nature Publishing Group. **e** Schematic diagram of experimental setup for monitoring beetle motion with μ-CE camera; **f** images of a free-crawling beetle at different time; **g** images obtained by μ-CE camera at different time; **h** schematic diagram of principle for 3D reconstruction by a μ-CE camera; **i** 3D reconstruction of paramecium motion trajectory. Reproduced with permission from Ref. [71]. Copyright 2022, Nature Publishing Group

demonstrate the real-time trajectory detection capability. The μ-CE camera captured a motion video of the paramecium and the trajectory was reconstructed in real-time at a rate of 24 frames per second (Fig. 7i). The above results confirmed the dynamic imaging capability of the μ-CE camera and showed promising prospects for real-time tracking monitoring, microscopic stereoscopic imaging, etc.

3.5 Wide spectral response

The human eye is capable of seeing light between 380 and 780 nm. Different wavelengths of light correspond to different colors, so we can see the colorful world. The reason why humans have color vision is that there are three types of cones in the retina that respond to red (L), green (M), and blue (S) light (Fig. 8a) [115]. Furthermore, stomatopod crustaceans or mantis shrimp may have the most sophisticated retinal photoreceptors in the animal kingdom. Through different arrangements of receptors, the retinas of mantis shrimp have more than a dozen photoreceptors. This allows them to see not only visible light but also ultraviolet light, giving them the widest spectrum recognition range of any animal (Fig. 8a). In addition, shrimp have polarization filters in their eyes and can directly see the polarization of incoming light [116].

Likewise, wide spectral response and specific wavelength detection are also essential for bioinspired curved vision systems, and much researches have been devoted to this area [56, 59, 62–64, 114, 117]. Thai et al. [62] achieved near infrared curved imaging by applying biaxial stretching to ultrathin molybdenum disulfide materials. The graphene/MoS_2/graphene metal–semiconductor-metal (MSM) photodetector array was fabricated on the flexible polyimide (PI) substrate. And the PI substrate could be bulged or dented into ellipses by controllable pneumatic bulging technique to apply the bisexual tensile stress. As demonstrated in Fig. 8b, significant deformation of the device could be observed, but no delamination or structural failure of MoS_2 and graphene occurred after deformation. The properties of the MoS_2 photodetector were then characterized before and after deformation. Owing to the narrow band gap ($\sim$ 1.9 eV), molybdenum disulfide materials had a limited spectral response range (visible light). As shown in Fig. 8c, MoS_2 photodetectors did not respond to the light above 685 nm before the strain was applied. Under the effect of strain, the detection spectrum was extended to the infrared wavelength. A clear response at 904 nm could be found, which was because the strain changed the lattice symmetry of MoS_2 and led to a narrow band gap. In addition, as the strain increased, the device response at different wavelengths was also significantly improved. This could be due to the increase in absorption efficiency and carrier mobility of MoS_2. Finally, a 7×8 PD array was prepared for demonstration of curved imaging. Light with a wavelength of 785 nm was used to project the letter “E” on the mask onto the curved image sensor. When the strain was 1.19%, a clear image with the pattern of the letter “E” was obtained (Fig. 8d).

Compared with inorganic semiconductor, the organic semiconductor has excellent flexibility and simple preparation technology, which is very suitable for the construction of curved image sensor. However, limited by the high exciton binding energy (0.3–1 eV), the infrared detection performance of organic semiconductors is poor. Therefore, Yu et al. [63] proposed a novel composite dielectric layer that improved the exciton dissociation efficiency and reduced the dark current. Following this strategy, an ultraflexible all-polymer heterojunction near-infrared phototransistors (PTs) were constructed for bioinspired curved imaging. Figure 8e shows the structure of the transistor. DPPT-TT: N2200, Au, and PEDOT: PSS were used as the photosensitive active channel, source/drain electrode, and gate electrode, respectively. And the composite dielectric layer was composed of poly(methyl methacrylate) (PMMA), polyvinyl alcohol (PVA), and epoxy-based resin (PEI-EP), which played the roles of reducing dark current, avoiding solvent damage, and inducing phase separation, respectively. Figure 8f shows the ultraviolet–visible-infrared absorption spectra of different films. In particular, the DPPT-TT: N2200 film combined the properties of both materials and had a wide absorption range and strong absorption in the near-infrared region. Both DPPT-TT PT and DPPT-TT: N2200 PT exhibited a photoresponse at 808 nm. Compared with DPPT-TT PT, the photosensitivity (P) and responsivity (R) of DPPT-TT: N2200 PT were improved by at least 10 times (Fig. 8g). The highest P value was 106, higher than that of all reported organic thin-film NIR PTs. In addition, a 9×10 PT array was constructed. The PT array could be stretched into a curved image sensor due to the deformability of the ultrathin structure. As shown in Fig. 8h, the imaging result of the curved imager was clearer with high contrast and clear edges than that of the planar device.

In addition to the wide spectral response, the identification of specific wavelengths is also important for the curved vision system [118]. Feng et al. [64] implemented a hemispherical perovskite image sensor with a narrowband response from visible to near-infrared. The structure of the curved image sensor was shown in Fig. 8i. And Cr, PEDOT: PSS, perovskite, C60 and 2,9-dimethyl-4,7-diphenyl-1,10-phenanthroline (BCP) acted as electrodes, the hole transport layer, the photosensitive layer, the electron transport layer and the buffer layer, respectively. The most important part was the perovskite layer because its dynamic carrier behavior directly affected the narrowband response of the photodetector. Considering that 2D perovskite was evenly distributed around 3D perovskite in quasi-2D perovskite materials, the dynamic behavior of the carrier could be modified by adjusting the ratio of 2D/3D perovskite materials. Figure 8j confirms the feasibility of this method. By changing the I/Br ratio and the thickness of the perovskite film, the light penetration depth and the carrier diffusion length could be adjusted. Continuous tuning of the external quantum efficiency (EQE) spectrum from the visible to the near-infrared could be achieved with

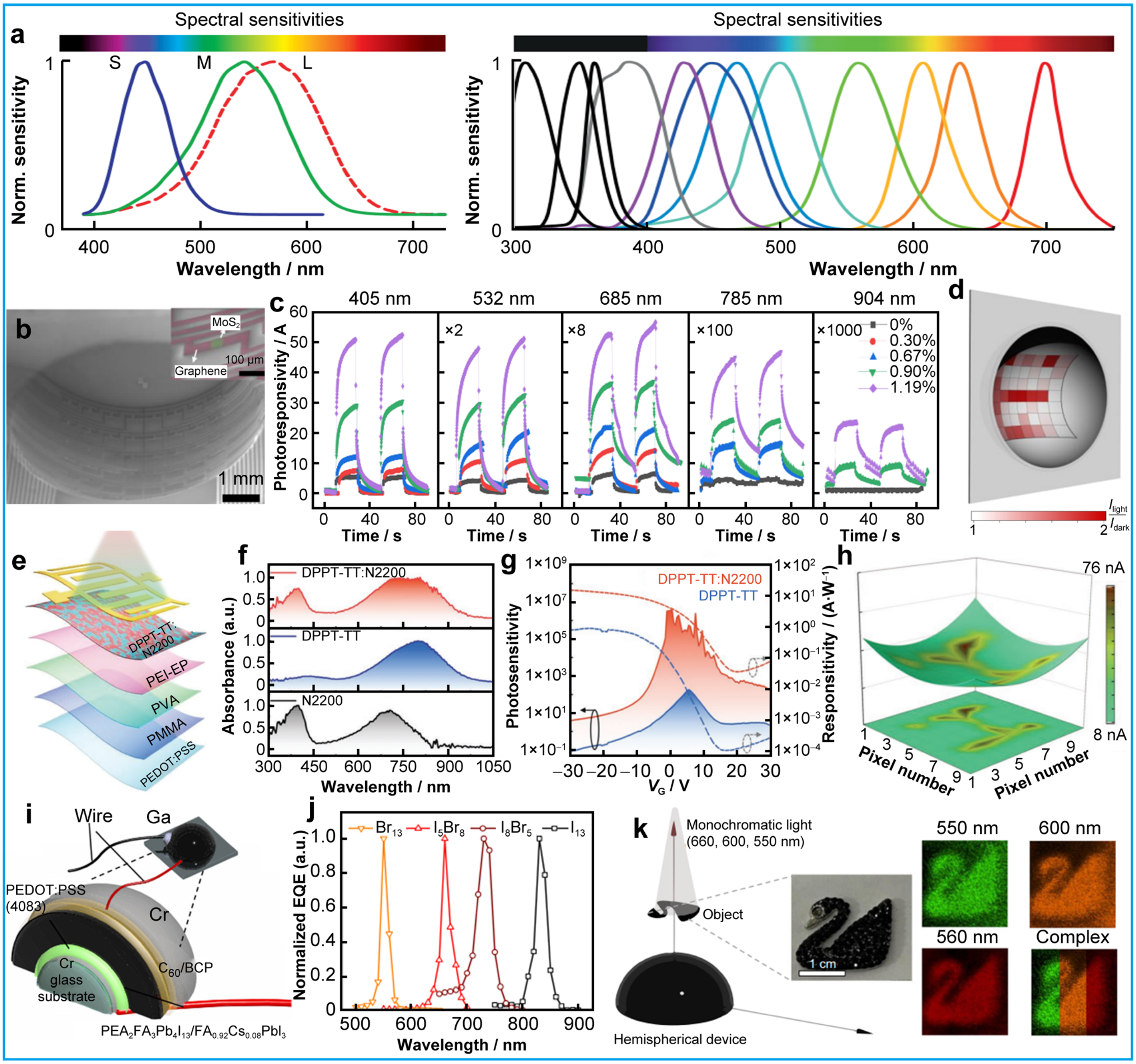

Fig. 8 **a** Photoreceptor spectral sensitivities of human and N. oerstedii. Reproduced with permission from Ref. [115]. Copyright 2008, Humana Press, a part of Springer Science Business Media. Reproduced with permission from Ref. [116]. Copyright 2022, Royal Society. **b** SEM image of planar device protruded into hemispherical shape and (inset) enlarged SEM image; **c** strain-dependent photoresponsivities under different incident light; **d** image of letter 'E' captured by curved imager with 1.19% strain at 785 nm incident light. Reproduced with permission from Ref. [62]. Copyright 2021, American Chemical Society. **e** Structure diagram of flexible device; **f** normalized optical absorption spectra of original DPPT-TT, N2200, and DPPT-TT: N2200 (1:1) films coated on quartz substrates; **g** photosensitivity (P), responsivity (R) as a function of V_G, according to same light intensities (0.038 mW·cm^{-2}, 808 nm) under two different conditions (DPPT-TT: N2200 and pristine DPPT-TT); **h** image (letter 'H') captured by bioinspired camera and its projection on flat plane. Reproduced with permission from Ref. [63]. Copyright 2022, Wiley–VCH. **i** Schematic diagram of structure of a hemispherical photodetector; **j** narrow-band response (EQE) of perovskites photodetectors with different halogen ratios ($PEA_2FA_3Pb_4I_{13-x}Br_x$, x = 1, 5, 8, 13); **k** (left) schematic representation of an experimental setup for color imaging, and (right) images obtained by hemispherical photodetectors with different I/Br ratios. Reproduced with permission from Ref. [64]. Copyright 2022, Nature Publishing Group

full width at half maximums (FWHMs) less than 20 nm. Curved image sensors with selective response wavelengths of 550, 600 and 660 nm were fabricated to verify the spectral sensing capability. The experimental setup for the imaging test is shown in Fig. 8k (left). The images captured by the different curved image sensors with selected wavelengths are shown in Fig. 8k (right). By converting the EQE spectrum into RGB (red, green, blue) coordinates, the compositing color image was also obtained, illustrating the potency of color imaging.

Although narrow-band response photodetectors are capable of color recognition, discrete devices increase the difficulty of testing and data reading time. Song et al. [65] addressed this issue by fabricating intrinsically stretchable, multispectral, and multiplexed 5 × 5 × 3 phototransistor arrays that integrated three color-selective stretchable phototransistors together. The structure of the device was shown in Fig. 9a, where the semiconductor nanocomposite material (isQDSN) was composed of CdSe/ZnS core/shell quantum dots with adjustable size, the fiber-like semiconductor polymer (poly[2, 5-(2-octyldodecyl)-3,6-diketopyrrolopyrrole-alt-5,5-(2,5-di(thien-2-yl)thieno[3,2-b]thiophene)](PDPP2T-TT-OD)) for charge transport and the elastomer (polystyrene-block-poly(ethylene-ran-butylene)-block-polystyrene (SEBS)). To ensure the device's stretchability, SEBS and microcracked gold films were used as the medium and electrode, respectively. The stretchable multiplexed transistor array was obtained by asymmetrically integrating the red, green, and blue color selective 5 × 5 phototransistor arrays. Due to its intrinsic stretchability, the device could be transformed from flat to hemispherical under the action of the deformation table (Fig. 9b) while maintaining good electrical stability. The color selectivity of the phototransistor was shown in Fig. 9c. The phototransistor composed of sensitive to blue light isQDSN had an obvious response to blue light (450 nm) and a weak response to green light (525 nm) and red light (635 nm). The green transistor had a strong response to both blue and green lights but a weak response to red light. The red transistor responded to blue, green, and red light. To improve the accuracy of optical detection under curved structures, the deep neural network (DNN) algorithm was used to compensate for the optical difference and noise caused by device deformation (Fig. 9d), and color detection under the curved structure was realized (Fig. 9e).

When integrating a color selective device, three pixels output one color, which increases the process difficulty and reduces pixel density. Long et al. [66] implemented a bionic eye with filter-free color vision using color-dependent bidirectional synaptic photoreactivity in the hybrid nanostructure (Fig. 10a). The artificial retina consisted of the hybrid nanostructures assembled in a hemispherical PAM. The hybrid nanostructures were composed of $CsPbI_3$/NiO core–shell nanowires and SnO_2/NiO double-shell nanotubes with ionic liquid-filled cores, mimicking cones and neurons in the human eye, respectively (Fig. 10b). Figure 10c shows the optical response of the device under red, green and blue pulses at a voltage of 0 V. The photocurrent under red and green light was negative, and the photocurrent under green light was greater than that under red light. However, the photocurrent under blue light was positive. This phenomenon was caused by the optoelectronic surrounding gate effect in the nanowire structure. Based on this principle, the bionic eye could recognize color. To improve the color recognition ability of the bionic eye, a small external voltage was applied. Applying a positive bias could enhance the photocurrent under blue light, while applying a negative bias could enhance the photocurrent under red light. Thus, the color information could be read out by analyzing the light response at different bias voltages. A convolutional neural network (CNN) was introduced to improve the color image reconstruction ability (Fig. 10d). For verifying the color detection capabilities of the bionic eyes, images of different shapes and colors were projected onto the bionic eyes. The photocurrents were measured under different biases. After normalization and CNN processing, the reconstructed image showed high fidelity (Fig. 10e).

3.6 Amphibious imaging

Creatures living only in water or land have developed individual eye structures. In the atmospheric environment (refractive index ~ 1.0), the prominent cornea of the human eye plays a major role in the refractive effect. However, in water (refractive index ~ 1.33), the refractive effect of the cornea is lost because the refractive index of water and the biological fluid in the eye are very similar. The refraction of the lens and vitreous body is not enough to focus the light on the retina. The image falls behind the retina, resulting in farsightedness. For aquatic fish, the light refraction function is mainly provided by the spherical lens. The spherical cornea is not involved in refraction. However, if the cornea is in the atmospheric environment, it can play the role of refraction, leading to the short-sightedness of imaging in front of the retina. To be able to live in water and on land at the same time, one solution is to flatten the curvature of the cornea [4]. For example, fiddler crabs have flat corneas and gradient index lenses (Fig. 11a) [43]. Inspired by the amphibious fiddler crab eyes, Lee et al. [58] proposed an amphibious artificial vision system. The ommatidia of the fiddler crab were mainly composed of the gradient index corneal lens (GCL), the crystal cone (CC), and the screening pigment (SP) (Fig. 11b). In addition to the concave multilayer structure of the fiddler crab eye with a higher refractive index (RI) in the upper layer, another amphibious imaging structure with a flat roof in nature was the concave multilayer structure with a lower RI in the upper layer. Figure 11c shows the specific differences between them. According to the ray-tracing simulations of the two structures and the typical lens structure with a convex top, the two multilayer structures with gradient RI and the planar roof had the same focal length in both air

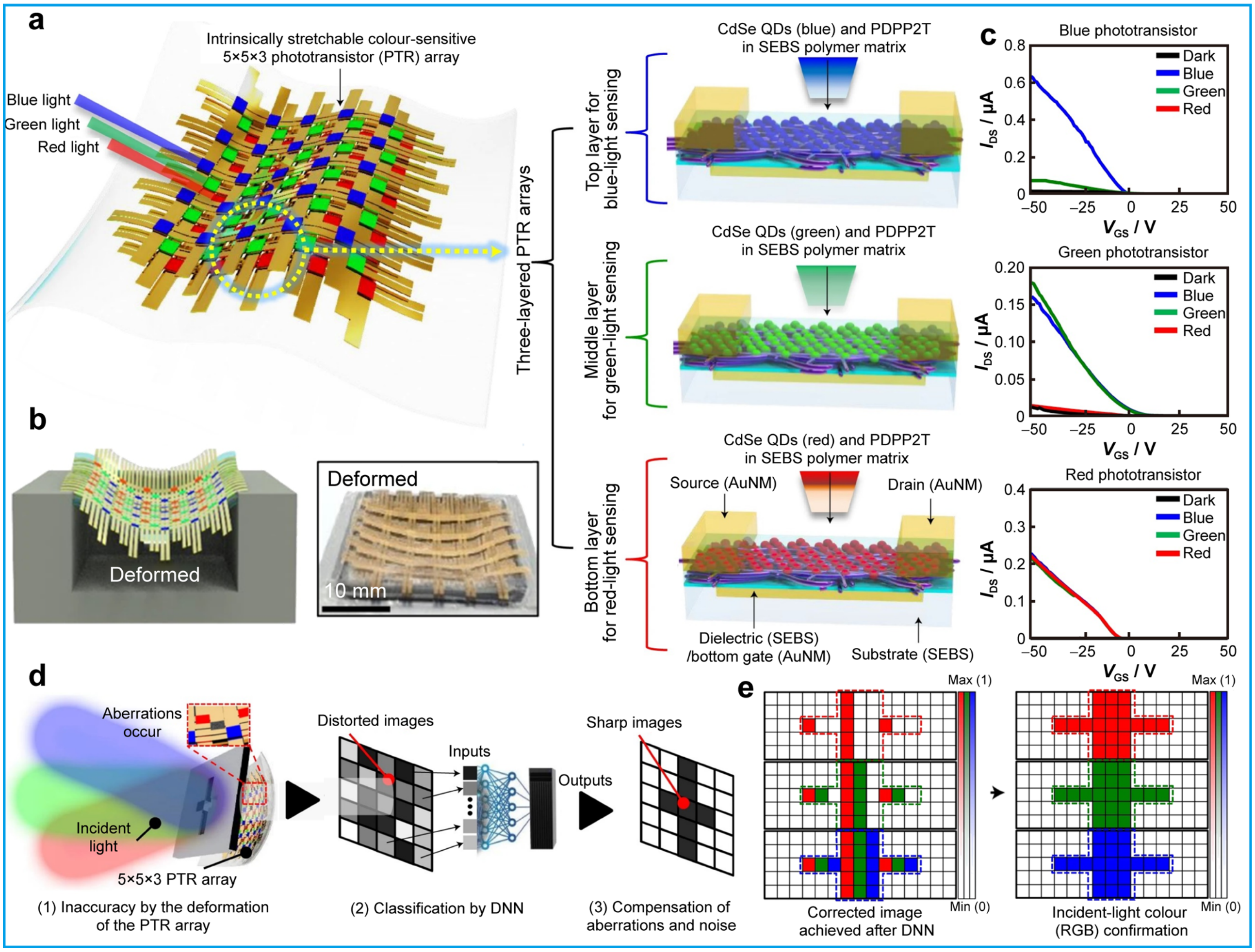

Fig. 9 **a** Schematic diagram of stretchable phototransistor array; **b** schematic diagram and photograph of 5 × 5 × 3 phototransistor array deformation; **c** photoresponse of blue phototransistor (top), green phototransistor (middle) and red phototransistor (bottom); **d** schematic diagram of using deep learning algorithm to improve accuracy of phototransistor during mechanical deformation; **e** corrected image pattern obtained after DNN processing (left), and incident light color confirmed by color-sensing algorithm (right). Reproduced with permission from Ref. [65]. Copyright 2022, Nature Publishing Group

and water, but the focal length of the traditional homogeneous convex lens changed (Fig. 11d). Therefore, the key to amphibious imaging was the planar roof and the gradient RI. Artificial ommatidia with the structure similar to amphibious fiddler crab eyes were also prepared as shown in Fig. 11e. The planar gradient lens (g-ML), polyurethane (PU) elastic spacer, and Si photodetector corresponded to the GCL, CC, and PR of the compound eyes of the fiddler crab. Considering the different preparation difficulty of the two structures and the anti-reflection effect of a convex multilayer structure, the g-ML structure with convex multilayer was adopted (Fig. 11f). Moreover, the artificial ommatidia were integrated into the three-dimensional spherical structure. Figure 11g presents the experimental device to demonstrate amphibious imaging. The artificial imaging system was partially placed in water, and two beams of light with square and circle patterns were illuminated on the device from air and water, respectively. As displayed in Fig. 11h, the images with clear square and circular patterns were obtained simultaneously, which verified the amphibious imaging function of the artificial compound eye.

4 Curved neuromorphic imaging systems

For image information acquisition and processing, traditional artificial vision systems require the integration of a large camera and a complex data processing module. It not only has a large volume and weight but also causes huge power consumption and data delay. In contrast, the curved retina in the human visual system with a small size can convert optical signals into electrical signals and has the function of data pre-processing. Therefore, it is of great

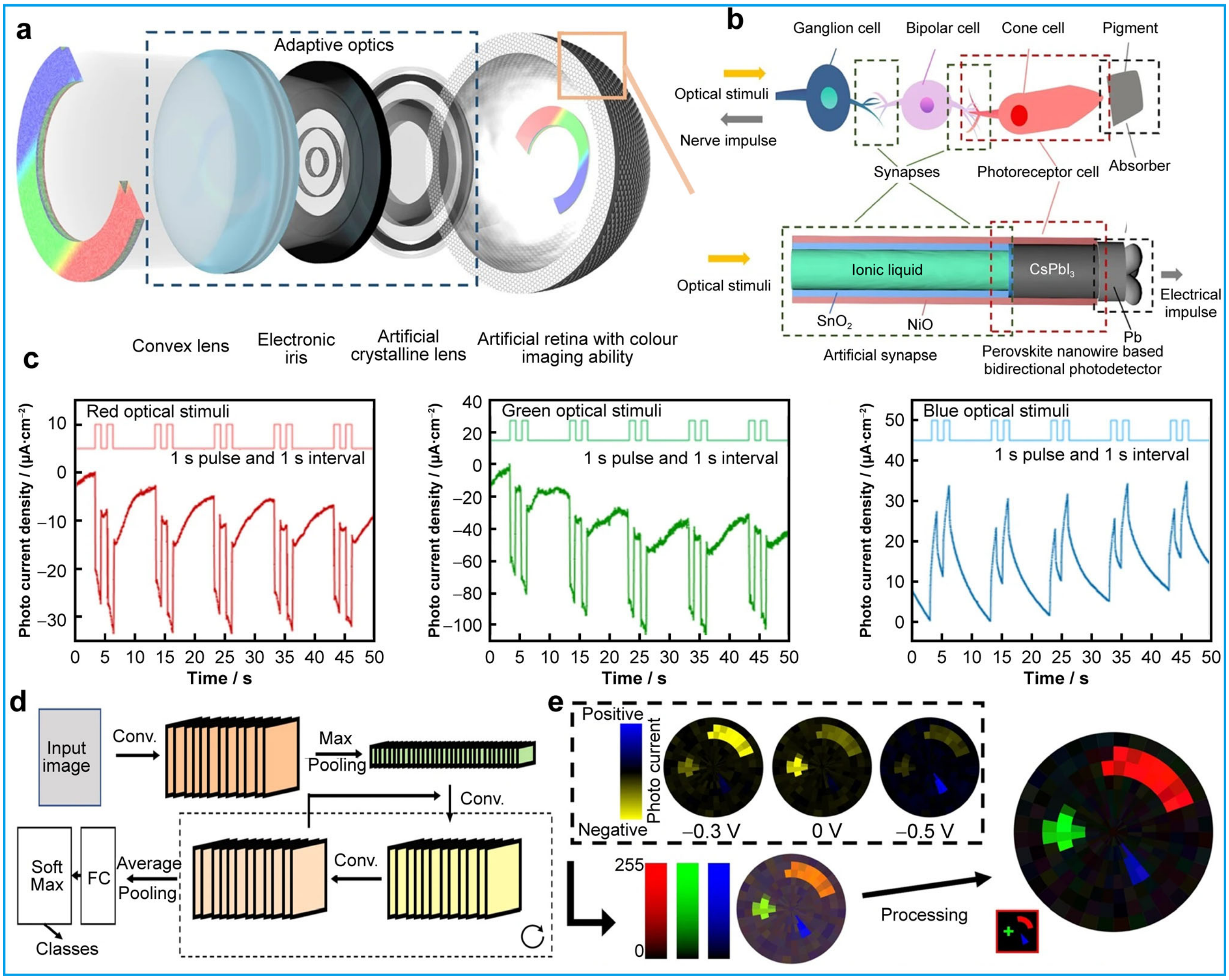

Fig. 10 **a** Schematic illustration of structure of bionic eye; **b** schematic diagrams of retinal neurons (top) and hybrid nanowires (below); **c** photocurrent density under 11 mW·cm^{-2} red (650 nm) (left), green (520 nm) (middle), and blue (405 nm) (right) illumination with 1 s pulse width and 1 s pulse interval for 5 cycles under 0 V bias; **d** architecture of CNN for image classification; **e** demonstration of color pattern reconstruction. Reproduced with permission from Ref. [66]. Copyright 2023, Nature Publishing Group

importance to develop a curved neuromorphic imaging system that combines bioinspired optical and neuromorphic processing functions.

4.1 Curved artificial optoelectronic synapses array

To mimic the neuromorphic computation of the human brain, synaptic devices have been extensively studied [28, 119–128]. However, the current synaptic devices are mostly limited to planar structures and rarely possess retina-like curved structures. Inspired by the human visual system, Choi et al. [129] first applied synapses to curved image sensors to obtain artificial neuromorphic vision systems. Notably, the curved structure could reduce the use of complex optical systems for imaging, and the synaptic plasticity could realize efficient data pre-processing. Figure 12a shows the structure of the MoS_2-pV3D3 phototransistor (pV3D3-PTr) with synaptic plasticity. It was made of a Si_3N_4 substrate, a graphene source/leak electrode, a MoS_2 photosensitive layer, a pV3D3 dielectric layer, and a Ti/Au gate electrode. The device exhibited short-term plasticity (Fig. 12b) to long-term potentiation (Fig. 12c) as the increase in the frequency of the input pulse light. The synaptic plasticity resulted from the charge trapping at the MoS_2-pV3D3 interface. Thus, the phototransistor exhibited quasi-linear time-dependent photocurrent generation and prolonged photocurrent decay. Based on the synaptic property, pV3D3-PTr could directly process the input optical signals and output the results in the form of electrical signals. Using the ultrathin structure and flexibility of the material, the pV3D3-PTr array was obtained with a curved structure. It was then integrated

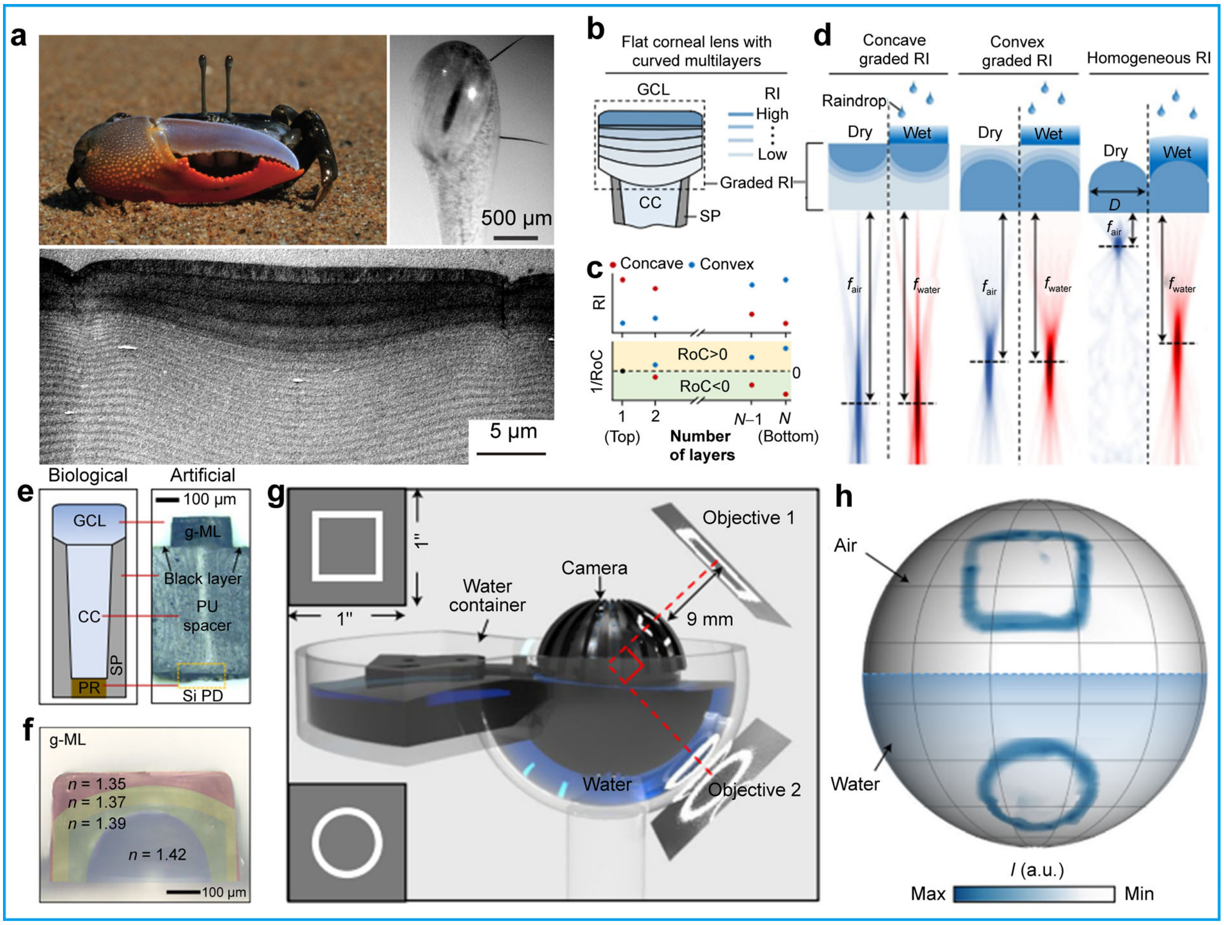

Fig. 11 **a** Optical photographs of U. vomeris and its compound eye (top), cross-sectional electron micrograph of a single lens in an ommatidium (below). Reproduced with permission from Ref. [43]. Copyright 2013, Wiley–VCH. **b** Schematic diagram of structure of ommatidium; **c** change of RI and RoC with number of layers in concavely and convexly curved multilayer structure; **d** ray-tracing optical simulation results of microlens with concave multilayers with graded RI (left), convex multilayers with graded RI (center), and typical microlens with a homogeneous RI (right) under dry and wet conditions; **e** structure of artificial (right) ommatidium and corresponding structure of biological ommatidium; **f** magnified cross-section view of g-ML; **g** schematic representation of experimental setup for amphibious imaging; **h** amphibious imaging results captured by artificial vision system. Reproduced with permission from Ref. [58]. Copyright 2022, Nature Publishing Group

with a plano-convex lens to achieve a curved vision system. Figure 12d–g demonstrates the image acquisition and data pre-processing of the imaging system. Specifically, the optical signal with a pattern of the letter “C” (e.g., 0.5 s duration and 0.5 s interval) was used as the input pulse signal. The photocurrent of the pixels in the frequently irradiated area gradually increased (Fig. 12f (i)). Meanwhile, the current of the pixels in the rarely irradiated area was negligible (Fig. 12g (i)). After 20 optical pulses, the pre-processed image “C” could be obtained and held for about 30 s (Fig. 12f (ii)). In addition, the image information could be erased by applying a forward bias (Fig. 12d–g (iii)) for the next imaging (Fig. 12d–g (iv)). This highly integrated curved vision system provides the future direction for the development of efficient machine vision.

Hu et al. [130] used MoS_2 to fabricate another hemispherical-structured bioinspired eye with optical synaptic function. (Fig. 12h). The traditional MoS_2 synaptic devices had significant power consumption, which was much higher than that of biological synapses. Hu et al. [130] introduced a discontinuous In layer to improve the contact between the electrode and MoS_2 and the conductivity of MoS_2, reducing the power consumption per spike to 68.9 aJ. In addition, the In/MoS_2 synaptic devices demonstrated synaptic plasticity, including the response to the pulse facilitation phenomenon, short-term plasticity, long-term plasticity, and the conversion between the two. Subsequently, MoS_2 thin films and discontinuous In layers were deposited directly on the quartz hemisphere shell in sequence to

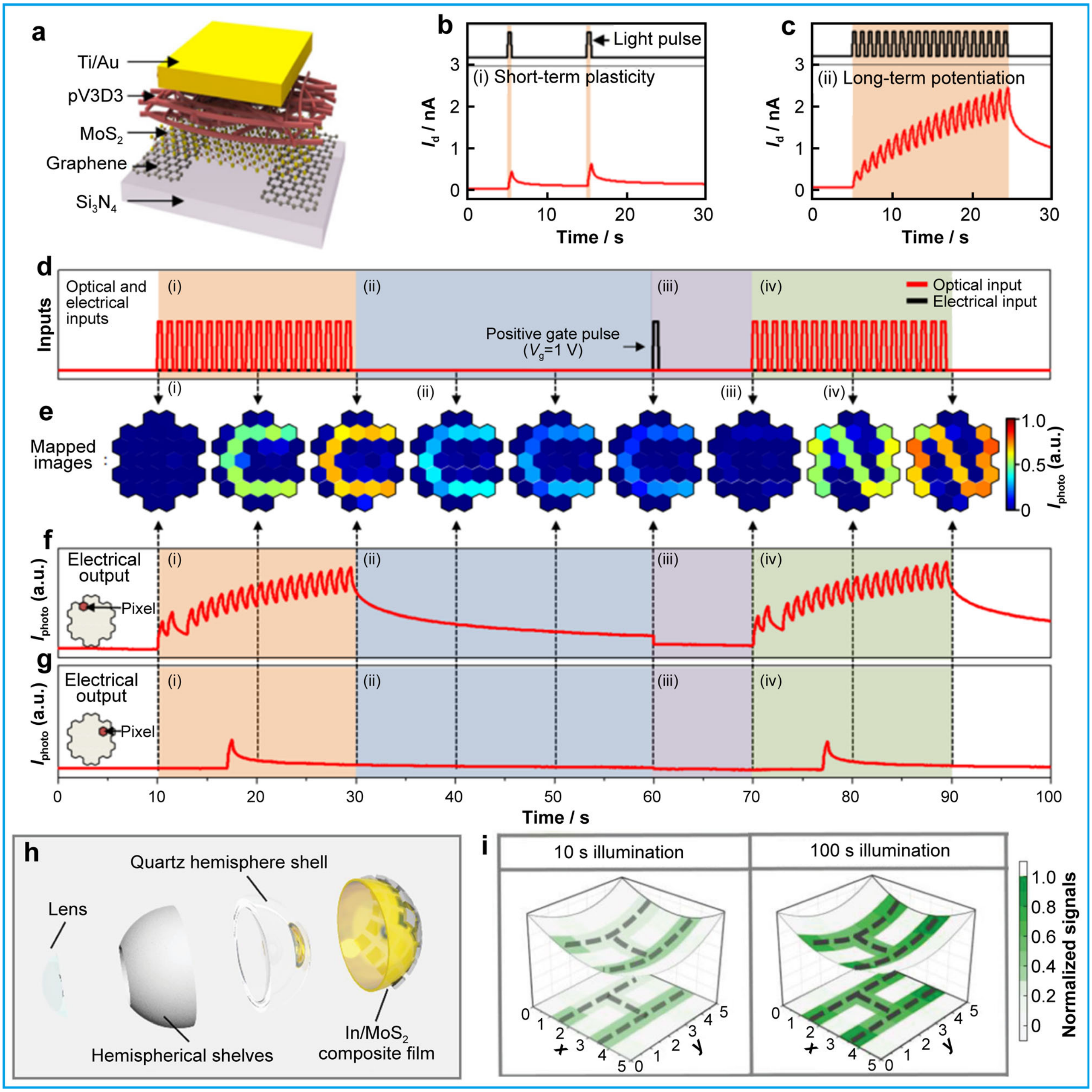

Fig. 12 **a** Schematic illustration of structure of pV3D3-PTr; **b** photon-triggered short-term plasticity and **c** long-term potentiation of pV3D3-PTr; **d–g** demonstrations of a preprocessed image derived from a large number of noisy optical inputs (e.g., acquisition of preprocessed image of letter "C" (i), attenuation of memorized image of letter "C" (ii), erasure of afterimage (iii), and acquisition of preprocessed image of letter "N" (iv)). Reproduced with permission from Ref. [129]. Copyright 2020, Nature Publishing Group. **h** Schematic illustration of structure of bioinspired eye; **i** images captured by bioinspired eye under 10 and 100 s illumination. Reproduced with permission from Ref. [130]. Copyright 2021, Wiley–VCH

obtain a 5 × 5 synapse array on the curved surface, and it was assembled with the lens and hemisphere shell to achieve a hemispherical bioinspired eye. To demonstrate the learning function of the device, the pattern of the letter "H" was irradiated to the bionic eye for different durations (Fig. 12i). As the exposure time increased from 10 to 100 s, the device current increased significantly and the image pattern became clearer. It was confirmed that the hemispherical bionic eye could recognize images by increasing the illumination time.

4.2 Curved neuromorphic system with image storage

Obviously, storage is another necessary function of curved neuromorphic imaging systems [131–140]. The photomemory transistor combines the functions of transistor, photodetector, and memristor devices. It can not only reduce the complexity of the imaging system but also record the optical information in real time. Therefore, Kim et al. [141] constructed a hemispherical imaging system based on organic photomemory transistors. Figure 13a shows the microscopic optical picture of the transistor with the bottom-gate bottom-contact structure. Figure 13a, b is the schematic illustration of the corresponding cross-section. The whole device could be divided into eight layers from bottom to top, which were SiN_x rigid island, polyimide flexible substrate, Ti/Au/Ti grid, $HfO_2/Ta_2O_5/HfO_2$ inorganic dielectric layer, Ti/Au source/drain electrode, semiconductor insulator (SU-8 3 μm), the organic semiconductor layer (Pentacene), and Parylene passivation layer. In Fig. 13c, the transistor had a memory capacity due to the charge trapping in the grid dielectric. The grid dielectric could be divided into a blocking layer, a charge trapping layer, and a tunneling layer (Fig. 13d). In particular, when a high positive gate voltage was applied with light exposure, the Pentacene absorbed photons to produce photogenerated electrons (Fig. 13e). The electrons were able to tunnel through the tunneling layer and be trapped in the charge trapping layer. When the gate voltage was removed, the electrons remained trapped in the charge-captured layer, which shifted the threshold voltage, resulting in the optical memory effect (Fig. 13f). To remove the stored information, it was necessary to reset by applying a large negative grid voltage to remove or neutralize the trapped electrons (Fig. 13g). Figure 13c shows that the greater the light absorption is, the greater the

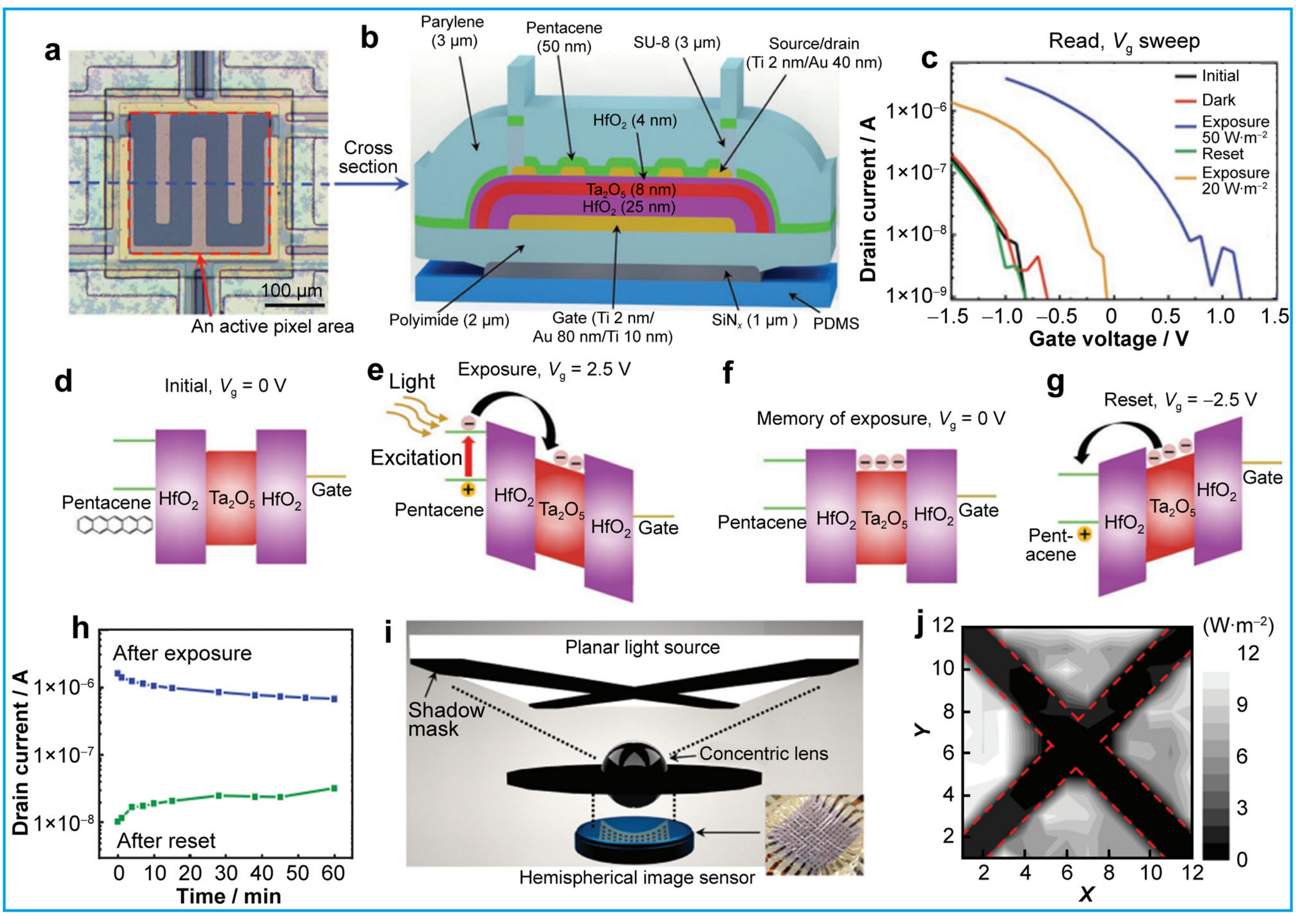

Fig. 13 **a** Optical image of organic photomemory transistor; **b** schematic illustration of cross-section of a photomemory transistor; **c** influence of illumination on threshold voltage of photomemory transistor; **d** initial state of photomemory transistor; **e** photogenerated charge carriers are produced under light, and photogenerated elMectrons are captured by trapping layer, resulting in a large positive grid voltage; **f** captured electrons are stored in trapping layer and cause a memory effect; **g** applying a high negative gate voltage can repulse and remove trapped electrons; **h** retention of drain currents after exposure and reset; **i** schematic representation of experimental setup for curved imaging; **j** image of letter “X” captured by curved image sensor array. Reproduced with permission from Ref. [141]. Copyright 2023, Wiley–VCH

threshold voltage shift of the transistor is. After resetting, the threshold voltage would return to its original value. Benefiting from the inorganic lattice dielectric layer, the charge storage effect could be maintained for more than 60 min (Fig. 13h). In addition, the 12 $\times$ 12 transistor array fabricated on a flat wafer was released and transferred to a pre-stretched hemispherical elastomer. After release, the image sensor buckled under compressive stress. The transistor array formed a curved image sensor for curved imaging (Fig. 13i). The image "X" was focused on the curved image sensor with a lens. After exposure, the light source was removed and the drain current of each pixel was read at voltages of $V_{\mathrm{g}} = -1$ V and $V_{\mathrm{d}} = -1.5$ V. The original image "X" was successfully reconstructed, as displayed in Fig. 13j. In this work, the construction of photomemory transistors not only reduced the complexity of imaging systems, but also provided a degree of freedom in the timing of imaging tests due to their memory function.

5 Summary

Over tens of thousands of years, creatures in different environments have evolved eyes with different structures and functions to adapt to their surroundings. Although all types of eyes differ in composition and working mechanism, they all share similar curved structures. The curved imaging structure can directly compensate for the aberration of the planar imaging system and reduce its structural complexity. Therefore, bioinspired curved imaging system with inheriting various functions of biological eyes, such as dynamic imaging, adjustable focus, and amphibious imaging, can surpass the traditional CCD and CMOS planar image sensors that work with complex structure and huge volume. In this review, we provide a systematic summary of the structures, functions, and neuromorphic systems of biological eyes, as well as the applications of bioinspired curved vision systems in imaging technology.

Inspired by various biological eyes, the development of curved imaging systems is advancing rapidly, but further improvements are needed in terms of resolution, pixel number, and spectral recognition.

(1) Currently, the curved vision system has an excellent optical structure in comparison with the planar vision system. However, the resolution and the number of pixels in the curved vision system are much lower than those of the planar image sensor. Curved image sensors are usually prepared by in-situ growth or planar structure curving techniques. For example, in situ growth of perovskite microwires can achieve high densities exceeding those of human retinal photoreceptor cells, however, the wiring of the electrodes in this structure is challenging. Furthermore, although bendable planar structures, such as ultrathin flexible structures, island bridge structures, kirigami structures, and origami structures, can be compatible with mature planar processing technology, high-resolution devices are not obtained due to complex integration processes. The kirigami structure has a large pixel filling factor, but cannot reach the resolution of the planar sensor. Combining a curved optical structure with a planar sensor can result in higher resolution, but the actual number of pixels is limited due to the small size of the device. Therefore, it is urgent to further improve the resolution and number of pixels of the curved surface imaging system for its practical application. The development of a preparation method that is compatible with mature planar processing technology represents the most promising direction for the advancement of curved imaging. Among the various approaches, the kirigami structure currently exhibits the highest pixel filling factor and has demonstrated curved imaging with 32 $\times$ 32 pixels, indicating its potential in the development of curved imaging. Another promising direction is to leverage the high resolution of planar image sensors by either increasing the size of the curved optical structure or designing special optical structures. By exploiting the benefits of planar processing technology and innovative optical designs, curved imaging can be further enhanced to deliver improved performance, functionality, and versatility in a range of fields.

(2) Compared to human vision, curved vision systems have a wide spectral response range, spanning from ultraviolet to infrared bands, due to semiconductor materials with abundant bandgaps. However, achieving color recognition remains a challenge for curved image sensors. Traditional flat camera uses a Bayer filter to achieve color recognition, however, this method is difficult to implement on a curved structure. Another approach involves using narrowband image sensors that respond to a specific wavelength, which has been used to enable color recognition of curved vision systems. However, integrating multiple narrowband devices into a single curved sensor is a complicated process, requiring several devices to detect the same target and then information integration to obtain a color image, which could be inefficient and slow. Integrating different color-selective photodetectors to enable color recognition represents a promising direction for the development of image sensors. However, the current pixel resolution achieved with such sensors, which require at least

three pixels (RGB) to determine a color, is relatively low, with a pitch of around 1 cm. One approach to improving the pixel resolution of image sensors is to use photodetectors that respond differently to various wavelengths of light. In this case, the color information of a pixel can be extracted by analyzing the measured current of the pixel under different bias conditions. By allowing each pixel to provide one color information instead of relying on multiple pixels to provide a single color, the resolution can be greatly improved. This approach imposes significant requirements on both device structure and the fabrication techniques, which may bring a paradigm shift in image sensors.

In short, biological eyes have many peculiar functions, such as the ability of shrimps to detect the polarization of light, cuttlefish to change the shape of their eyes to increase the focusing range, and the regeneration capability of crab eyes. Inspired by these remarkable functions, the improvement of curved vision systems requires further research. By emulating biological eyes, the imaging system could obtain enhanced performance and more comprehensive capabilities. Biomimicry could be the development direction of the imaging system in the future.

Acknowledgements This work was financially supported by the National Natural Science Foundation of China (Nos. 52125205, U20A20166, 61805015 and 61804011, 52102184, 52202181), the National key R&D program of China (Nos. 2021YFB3200302 and 2021YFB3200304) and the Fundamental Research Funds for the Central Universities.

Declarations

Conflict of interests The authors declare that they have no conflict of interest.

References

[1] Li PF, Fang Q, Wu YZ, Ji HL. Review of Subjective evaluation method of high-quality TV images. In: SID Symposium Digest of Technical Papers. 2022;53 Suppl 1:142. https://doi.org/10.1002/sdtp.15873

[2] Atchison DA, Smith G. Optics of the Human Eye. Oxford: Butterworth-Heinemann Oxford; 2000. 25.

[3] Fernald RD. Casting a genetic light on the evolution of eyes. Science. 2006;313(5795):1914. https://doi.org/10.1126/science.1127889.

[4] Land MF. The optics of animal eyes. Contemp Phys. 1988; 29(5):435. https://doi.org/10.1080/00107518808222601.

[5] Lakshminarayanan V, Kuppuswamy Parthasarathy M. Biomimetic optics: visual systems. J Mod Optic. 2016. https://doi.org/10.1080/09500340.2016.1224939.

[6] Bruckner A, Duparre J, Dannberg P, Brauer A, Tunnermann A. Artificial neural superposition eye. Opt Express. 2007;15(19): 11922. https://doi.org/10.1364/oe.15.011922.

[7] Duparré J, Dannberg P, Schreiber P, Bräuer A, Tünnermann A. Thin compound-eye camera. Appl Opt. 2005;44(15):2949. https://doi.org/10.1364/AO.44.002949.

[8] Chung T, Lee Y, Yang SP, Kim K, Kang BH, Jeong KH. Mining the smartness of insect ultrastructures for advanced imaging and illumination. Adv Funct Mater. 2018;28(24): 1705912. https://doi.org/10.1002/adfm.201705912.

[9] Guenter B, Joshi N, Stoakley R, Keefe A, Geary K, Freeman R, Hundley J, Patterson P, Hammon D, Herrera G, Sherman E, Nowak A, Schubert R, Brewer P, Yang L, Mott R, McKnight G. Highly curved image sensors: a practical approach for improved optical performance. Opt Express. 2017;25(12): 13010. https://doi.org/10.1364/oe.25.013010.

[10] Rim SB, Catrysse PB, Dinyari R, Huang K, Peumans P. The optical advantages of curved focal plane arrays. Opt Express. 2008;16(7):4965. https://doi.org/10.1364/OE.16.004965.

[11] Milojkovic P, Mait JN. Space-bandwidth scaling for wide field-of-view imaging. Appl Opt. 2012;51(4):A36. https://doi.org/10.1364/ao.51.000a36.

[12] Reshidko D, Sasian J. Optical analysis of miniature lenses with curved imaging surfaces. Appl Opt. 2015;54(28):E216. https://doi.org/10.1364/ao.54.00e216.

[13] Stamenov I, Agurok IP, Ford JE. Optimization of two-glass monocentric lenses for compact panoramic imagers: general aberration analysis and specific designs. Appl Opt. 2012; 51(31):7648. https://doi.org/10.1364/ao.51.007648.

[14] Land MF, Nilsson DE. Animal Eyes. Oxford: OUP Oxford; 2012. 72.

[15] Land MF. The optical structures of animal eyes. Curr Biol. 2005;15(9):R319. https://doi.org/10.1016/j.cub.2005.04.041.

[16] Vannier J, Schoenemann B, Gillot T, Charbonnier S, Clarkson E. Exceptional preservation of eye structure in arthropod visual predators from the Middle Jurassic. Nat Commun. 2016;7(1): 10320. https://doi.org/10.1038/ncomms10320.

[17] Howell KJ, Beston SM, Stearns S, Walsh MR. Coordinated evolution of brain size, structure, and eye size in Trinidadian killifish. Ecol Evol. 2021;11(1):365. https://doi.org/10.1002/ece3.7051.

[18] Xiao X, Xiao X, Lan Y, Chen J. Learning from nature for healthcare, energy, and environment. Innov. 2021;2(3):100135. https://doi.org/10.1016/j.xinn.2021.100135.

[19] Zhang ZJ, Xiao X, Zhou YH, Huang LJ, Wang YX, Rong QL, Han ZY, Qu HJ, Zhu ZJ, Xu SM, Tang JG, Chen J. Bioinspired graphene oxide membranes with ph-responsive nanochannels for high-performance nanofiltration. ACS Nano. 2021;15(8): 13178. https://doi.org/10.1021/acsnano.1c02719.

[20] Nikiforov-Nikishin DL, Irkha VA, Kochetkov NI, Kalita TL, Nikiforov-Nikishin AL, Blokhin EE, Antipov SS, Makarenkov DA, Zhavnerov AN, Glebova IA, Smorodinskaya SV, Chebotarev SN. Some aspects of development and histological structure of the visual system of Nothobranchius Guentheri. Animals. 2021;11(9):2755. https://doi.org/10.3390/ani11092755.

[21] Jeong KH, Kim J, Lee LP. Biologically inspired artificial compound eyes. Science. 2006;312(5773):557. https://doi.org/10.1126/science.1123053.

[22] Reyer RW. The Amphibian Eye: Development and Regeneration. Edited by Crescitelli F, Dvorak CA, Eder DJ, Granda AM, Hamasaki D, Holmberg K, Hughes A, Locket NA, McFarland WN, Meyer DB, Muntz WRA, Munz FW, Olson EC, Reyer RW, Crescitelli F. Berlin, Heidelberg: Springer Berlin Heidelberg 1977. 309

[23] Koretz JR, Cook CA, Kaufman PL. Aging of the human lens: changes in lens shape upon accommodation and with accommodative loss. J Opt Soc Am A. 2002;19(1):144. https://doi.org/10.1364/josaa.19.000144.

[24] Lopez-Gil N, Fernandez-Sanchez V. The change of spherical aberration during accommodation and its effect on the accommodation response. J Vision. 2010;10(13):12. https://doi.org/10.1167/10.13.12.

[25] Rossel S. Regional differences in photoreceptor performance in the eye of the praying mantis. J Comp Physiol. 1979;131(2):95. https://doi.org/10.1007/BF00619070.

[26] Zhou FC, Chai Y. Near-sensor and in-sensor computing. Nat Electron. 2020;3(11):664. https://doi.org/10.1038/s41928-020-00501-9.

[27] Tsai WL, Chen CY, Wen YT, Yang L, Cheng YL, Lin HW. Band tunable microcavity perovskite artificial human photoreceptors. Adv Mater. 2019;31(24):1900231. https://doi.org/10.1002/adma.201900231.

[28] Zhang ZH, Wang SY, Liu CS, Xie RZ, Hu WD, Zhou P. All-in-one two-dimensional retinomorphic hardware device for motion detection and recognition. Nat Nanotechnol. 2022;17(1):27. https://doi.org/10.1038/s41565-021-01003-1.

[29] Nilsson DE. Eye evolution and its functional basis. Vis Neurosci. 2013;30(1–2):5. https://doi.org/10.1017/s0952523813000035.

[30] Martin KAC, Scott K. Current opinion in neurobiology—sensory systems. Curr Opin Neurobiol. 2010;20(3):271. https://doi.org/10.1016/j.conb.2010.05.004.

[31] Gao WC, Xu ZS, Han X, Pan CF. Recent advances in curved image sensor arrays for bioinspired vision system. Nano Today. 2022;42:101366. https://doi.org/10.1016/j.nantod.2021.101366.

[32] Nassi JJ, Callaway EM. Parallel processing strategies of the primate visual system. Nat Rev Neurosci. 2009;10(5):360. https://doi.org/10.1038/nrn2619.

[33] Kogos LC, Li YZ, Liu JN, Li YY, Tian L, Paiella R. Plasmonic ommatidia for lensless compound-eye vision. Nat Commun. 2020;11(1):1637. https://doi.org/10.1038/s41467-020-15460-0.

[34] Meyer-Rochow VB. Compound eyes of insects and crustaceans: Some examples that show there is still a lot of work left to be done. Insect Sci. 2015;22(3):461. https://doi.org/10.1111/1744-7917.12117.

[35] Roorda A, Williams DR. The arrangement of the three cone classes in the living human eye. Nature. 1999;397(6719):520. https://doi.org/10.1038/17383.

[36] Rajagopal S, Roberts RD, Lim SK. Visible light communication: modulation schemes and dimming support. IEEE Commun Mag. 2012;50(3):72. https://doi.org/10.1109/mcom.2012.6163585.

[37] Martin GR. Form and Function in the Optical Structure of Bird Eyes. In: Davies MNO, Green PR, editors. Perception and Motor Control in Birds: An Ecological Approach. Heidelberg: Springer. 1994. 1.https://doi.org/10.1007/978-3-642-75869-0_2.

[38] Jagger WS, Sands PJ. A wide-angle gradient index optical model of the crystalline lens and eye of the octopus. Vision Res. 1999;39(17):2841. https://doi.org/10.1016/s0042-6989(99)00012-7.

[39] Cheng Y, Cao J, Zhang YK, Hao Q. Review of state-of-the-art artificial compound eye imaging systems. Bioinspir Biomim. 2019;14(3):031002. https://doi.org/10.1088/1748-3190/aaffb5.

[40] Floreano D, Zufferey JC, Srinivasan MV, Ellington C. Flying Insects and Robots. Heidelberg: Springer. 2009. 127.

[41] Dudley R. The Biomechanics of Insect Flight: Form, Function, Evolution. Princeton: Princeton University Press. 2002. 3.

[42] Herault J. Biologically Inspired Computer Vision: Fundamentals and Applications. Weinheim: Wiley. 2016. 111.

[43] Alkaladi A, Zeil J. Functional anatomy of the fiddler crab compound eye (Uca vomeris: Ocypodidae, Brachyura, Decapoda). J Comp Neurol. 2014;522(6):1264. https://doi.org/10.1002/cne.23472.

[44] Levy B, Sivak JG. Mechanisms of accommodation in the bird eye. J Comp Physiol. 1980;137(3):267. https://doi.org/10.1007/BF00657122.

[45] Euler T, Haverkamp S, Schubert T, Baden T. Retinal bipolar cells: elementary building blocks of vision. Nat Rev Neurosci. 2014;15(8):507. https://doi.org/10.1038/nrn3783.

[46] Pereda AE. Electrical synapses and their functional interactions with chemical synapses. Nat Rev Neurosci. 2014;15(4):250. https://doi.org/10.1038/nrn3708.

[47] Prezioso M, Merrikh-Bayat F, Hoskins BD, Adam GC, Likharev KK, Strukov DB. Training and operation of an integrated neuromorphic network based on metal-oxide memristors. Nature. 2015;521(7550):61. https://doi.org/10.1038/nature14441.

[48] Mayer M, Xiao X, Yin JY, Chen GR, Xu J, Chen J. Advances in bioinspired triboelectric nanogenerators. Adv Electron Mater. 2022;8(12):2200782. https://doi.org/10.1002/aelm.202200782.

[49] Xiao X, Yin JY, Chen GR, Shen S, Nashalian A, Chen J. Bioinspired acoustic textiles with nanoscale vibrations for wearable biomonitoring. Matter. 2022;5(5):1342. https://doi.org/10.1016/j.matt.2022.03.014.

[50] Zhang CH, Xiao X, Zhang YH, Liu ZX, Xiao X, Nashalian A, Wang XS, Cao MY, He XM, Chen J, Jiang L, Yu CM. Bioinspired anisotropic slippery cilia for stiffness-controllable bubble transport. ACS Nano. 2022;16(6):9348. https://doi.org/10.1021/acsnano.2c02093.

[51] Luo Y, Xiao X, Chen J, Li Q, Fu HY. Machine-learning-assisted recognition on bioinspired soft sensor arrays. ACS Nano. 2022;16(4):6734. https://doi.org/10.1021/acsnano.2c01548.

[52] Zan GT, Wu T, Zhang ZL, Li J, Zhou JC, Zhu F, Chen HX, Wen M, Yang XC, Peng XJ, Chen J, Wu QS. Bioinspired nanocomposites with self-adaptive stress dispersion for super-foldable electrodes. Adv Sci. 2022;9(3):2103714. https://doi.org/10.1002/advs.202103714.

[53] Zhou J, Huang H, Wang LJ, Tamaddon M, Liu CZ, Liu ZY, Yu TB, Zhang YZ. Stable mechanical fixation in a bionic osteochondral scaffold considering bone growth. Rare Met. 2022;41(8):2711. https://doi.org/10.1007/s12598-022-02000-6.

[54] Cai J, Chen HY, Li YJ, Akbarzadeh A. Lessons from nature for carbon-based nanoarchitected metamaterials. Small Sci. 2022;2(12):2200039. https://doi.org/10.1002/smsc.202200039.

[55] Wijerathne B, Liao T, Ostrikov K, Sun Z. Bioinspired robust mechanical properties for advanced materials. Small Struct. 2022;3(9):2100228. https://doi.org/10.1002/sstr.202100228.

[56] Kim M, Lee GJ, Choi C, Kim MS, Lee M, Liu S, Cho KW, Kim HM, Cho H, Choi MK, Lu N, Song YM, Kim DH. An aquatic-vision-inspired camera based on a monocentric lens and a silicon nanorod photodiode array. Nat Electron. 2020;3(9):546. https://doi.org/10.1038/s41928-020-0429-5.

[57] Song YM, Xie YZ, Malyarchuk V, Xiao JL, Jung I, Choi KJ, Liu ZJ, Park H, Lu CF, Kim RH, Li R, Crozier KB, Huang YG, Rogers JA. Digital cameras with designs inspired by the arthropod eye. Nature. 2013;497(7447):95. https://doi.org/10.1038/nature12083.

[58] Lee M, Lee GJ, Jang HJ, Joh E, Cho H, Kim MS, Kim HM, Kang KM, Lee JH, Kim M, Jang H, Yeo JE, Durand F, Lu N, Kim DH, Song YM. An amphibious artificial vision system with a panoramic visual field. Nat Electron. 2022;5(7):452. https://doi.org/10.1038/s41928-022-00789-9.

[59] Zhang K, Jung YH, Mikael S, Seo JH, Kim M, Mi HY, Zhou H, Xia ZY, Zhou WD, Gong SQ, Ma ZQ. Origami silicon optoelectronics for hemispherical electronic eye systems. Nat Commun. 2017;8(1):1782. https://doi.org/10.1038/s41467-017-01926-1.

[60] Rao ZY, Lu YT, Li ZW, Sim K, Ma ZQ, Xiao JL, Yu CJ. Curvy, shape-adaptive imagers based on printed optoelectronic

pixels with a kirigami design. Nat Electron. 2021;4(7):513. https://doi.org/10.1038/s41928-021-00600-1.

[61] Gu LL, Poddar S, Lin YJ, Long ZH, Zhang DQ, Zhang QP, Shu L, Qiu X, Kam M, Javey A, Fan ZY. A biomimetic eye with a hemispherical perovskite nanowire array retina. Nature. 2020; 581(7808):278. https://doi.org/10.1038/s41586-020-2285-x.

[62] Thai KY, Park I, Kim BJ, Hoang AT, Na Y, Park CU, Chae Y, Ahn JH. MoS_2/Graphene photodetector array with strain-modulated photoresponse up to the near-infrared regime. ACS Nano. 2021;15(8):12836. https://doi.org/10.1021/acsnano.1c04678.

[63] Yu HY, Zhao XL, Tan MY, Wang B, Zhang MX, Wang X, Guo SL, Tong YH, Tang QX, Liu YC. Ultraflexible and ultrasensitive near-infrared organic phototransistors for hemispherical biomimetic eyes. Adv Funct Mater. 2022;32(48): 2206765. https://doi.org/10.1002/adfm.202206765.

[64] Feng XP, He YH, Qu W, Song JM, Pan WT, Tan MR, Yang B, Wei HT. Spray-coated perovskite hemispherical photodetector featuring narrow-band and wide-angle imaging. Nat Commun. 2022;13(1):6106. https://doi.org/10.1038/s41467-022-33934-1.

[65] Song JK, Kim J, Yoon J, Koo JH, Jung H, Kang K, Sunwoo SH, Yoo S, Chang H, Jo J, Baek W, Lee S, Lee M, Kim HJ, Shin M, Yoo YJ, Song YM, Hyeon T, Kim DH, Son D. Stretchable colour-sensitive quantum dot nanocomposites for shape-tunable multiplexed phototransistor arrays. Nat Nanotechnol. 2022; 17(8):849. https://doi.org/10.1038/s41565-022-01160-x.

[66] Long ZH, Qiu X, Chan CLJ, Sun ZB, Yuan ZN, Poddar S, Zhang YT, Ding YC, Gu LL, Zhou Y, Tang WY, Srivastava AK, Yu CJ, Zou XM, Shen GZ, Fan ZY. A neuromorphic bionic eye with filter-free color vision using hemispherical perovskite nanowire array retina. Nat Commun. 2023;14(1): 1972. https://doi.org/10.1038/s41467-023-37581-y.

[67] Cao JJ, Hou ZS, Tian ZN, Hua JG, Zhang YL, Chen QD. Bioinspired zoom compound eyes enable variable-focus imaging. ACS Appl Mater Interfaces. 2020;12(9):10107. https://doi.org/10.1021/acsami.9b21008.

[68] Keum D, Jang KW, Jeon DS, Hwang CSH, Buschbeck EK, Kim MH, Jeong KH. Xenos peckii vision inspires an ultrathin digital camera. Light Sci Appl. 2018;7(1):80. https://doi.org/10.1038/s41377-018-0081-2.

[69] Shi CY, Wang YY, Liu CY, Wang TS, Zhang HX, Liao WX, Xu ZJ, Yu WX. SCECam: a spherical compound eye camera for fast location and recognition of objects at a large field of view. Opt Express. 2017;25(26):32333. https://doi.org/10.1364/oe.25.032333.

[70] Dai B, Zhang L, Zhao CL, Bachman H, Becker R, Mai J, Jiao Z, Li W, Zheng LL, Wan XJ, Huang TJ, Zhuang SL, Zhang D. Biomimetic apposition compound eye fabricated using microfluidic-assisted 3D printing. Nat Commun. 2021;12(1): 6458. https://doi.org/10.1038/s41467-021-26606-z.

[71] Hu ZY, Zhang YL, Pan C, Dou JY, Li ZZ, Tian ZN, Mao JW, Chen QD, Sun HB. Miniature optoelectronic compound eye camera. Nat Commun. 2022;13(1):5634. https://doi.org/10.1038/s41467-022-33072-8.

[72] Elbamby MS, Perfecto C, Bennis M, Doppler K. Toward low-latency and ultra-reliable virtual reality. IEEE Netw. 2018; 32(2):78. https://doi.org/10.1109/MNET.2018.1700268.

[73] Lee GJ, Choi C, Kim DH, Song YM. Bioinspired artificial eyes: optic components, digital cameras, and visual prostheses. Adv Funct Mater. 2018;28(24):1705202. https://doi.org/10.1002/adfm.201705202.

[74] Lee GJ, Nam WI, Song YM. Robustness of an artificially tailored fisheye imaging system with a curvilinear image surface. Opt Laser Technol. 2017;96:50. https://doi.org/10.1016/j.optlastec.2017.04.026.

[75] Jung IW, Xiao JL, Malyarchuk V, Lu CF, Li M, Liu ZJ, Yoon J, Huang YG, Rogers JA. Dynamically tunable hemispherical electronic eye camera system with adjustable zoom capability. P Natl Acad Sci USA. 2011;108(5):1788. https://doi.org/10.1073/pnas.1015440108.

[76] Wu T, Hamann SS, Ceballos AC, Chang CE, Solgaard O, Howe RT. Design and fabrication of silicon-tessellated structures for monocentric imagers. Microsyst Nanoeng. 2016;2(1): 16019. https://doi.org/10.1038/micronano.2016.19.

[77] Kingslake R, Johnson RB. Lens Design Fundamentals. Oxford: Academic Press. 2009. 1.

[78] Jagger WS. The optics of the spherical fish lens. Vision Res. 1992;32(7):1271. https://doi.org/10.1016/0042-6989(92)90222-5.

[79] Sivak JG. Optical Variability of the Fish Lens. In: Douglas R, Djamgoz M, editors. The Visual System of Fish. Dordrecht: Springer. 1990. 1. https://doi.org/10.1007/978-94-009-0411-8_3.

[80] Buschbeck EK, Ehmer B, Hoy RR. Chunk versus point sampling: visual imaging in a small insect. Science. 1999; 286(5442):1178. https://doi.org/10.1126/science.286.5442.1178.

[81] Buschbeck EK, Ehmer B, Hoy RR. The unusual visual system of the Strepsiptera: external eye and neuropils. J Comp Physiol A. 2003;189(8):617. https://doi.org/10.1007/s00359-003-0443-x.

[82] Maksimovic S, Layne JE, Buschbeck EK. Behavioral evidence for within-eyelet resolution in twisted-winged insects (Strepsiptera). J Exp Biol. 2007;210(16):2819. https://doi.org/10.1242/jeb.004697.

[83] Zhai YQ, Niu JQ, Liu JQ, Yang B. High numerical aperture imaging systems formed by integrating bionic artificial compound eyes on a CMOS sensor. Opt Mater Express. 2021; 11(6):1824. https://doi.org/10.1364/ome.427623.

[84] Zhang YH, Yan Z, Nan KW, Xiao DQ, Liu YH, Luan HW, Fu HR, Wang XZ, Yang QL, Wang JC, Ren W, Si HZ, Liu F, Yang LH, Li HJ, Wang JT, Guo XL, Luo HY, Wang L, Huang YG, Rogers JA. A mechanically driven form of Kirigami as a route to 3D mesostructures in micro/nanomembranes. P Natl Acad Sci USA. 2015;112(38):11757. https://doi.org/10.1073/pnas.1515602112.

[85] Liu WJ, Zou QS, Zheng CQ, Jin CJ. Metal-assisted transfer strategy for construction of 2D and 3D nanostructures on an elastic substrate. ACS Nano. 2019;13(1):440. https://doi.org/10.1021/acsnano.8b06623.

[86] Zhao HB, Li K, Han MD, Zhu F, Vazquez-Guardado A, Guo PJ, Xie ZQ, Park Y, Chen L, Wang XJ, Luan HW, Yang YY, Wang HL, Liang CM, Xue YG, Schaller RD, Chanda D, Huang YG, Zhang YH, Rogers JA. Buckling and twisting of advanced materials into morphable 3D mesostructures. P Natl Acad Sci Usa. 2019;116(27):13239. https://doi.org/10.1073/pnas.1901193116.

[87] Xu S, Zhang Y, Cho J, Lee J, Huang X, Jia L, Fan JA, Su Y, Su J, Zhang H, Cheng H, Lu B, Yu C, Chuang C, Kim T-i, Song T, Shigeta K, Kang S, Dagdeviren C, Petrov I, Braun PV, Huang Y, Paik U, Rogers JA. Stretchable batteries with self-similar serpentine interconnects and integrated wireless recharging systems. Nat Commun. 2013;4(1):1543. https://doi.org/10.1038/ncomms2553.

[88] Chen YC, Lu YJ, Liao MY, Tian YZ, Liu Q, Gao CJ, Yang X, Shan CX. 3D Solar-blind Ga2O3 photodetector array realized via origami method. Adv Funct Mater. 2019;29(50):1906040. https://doi.org/10.1002/adfm.201906040.

[89] Lee W, Liu Y, Lee Y, Sharma BK, Shinde SM, Kim SD, Nan K, Yan Z, Han M, Huang Y, Zhang Y, Ahn JH, Rogers JA. Two-dimensional materials in functional three-dimensional architectures with applications in photodetection and imaging. Nat Commun. 2018;9(1):1417. https://doi.org/10.1038/s41467-018-03870-0.

[90] Choi C, Choi MK, Liu S, Kim M, Park OK, Im C, Kim J, Qin X, Lee GJ, Cho KW, Kim M, Joh E, Lee J, Son D, Kwon SH,

Jeon NL, Song YM, Lu N, Kim DH. Human eye-inspired soft optoelectronic device using high-density MoS_2-graphene curved image sensor array. Nat Commun. 2017;8(1):1664. https://doi.org/10.1038/s41467-017-01824-6.
[91] Li JF, Liu ZG. Focused-ion-beam-based nano-kirigami: from art to photonics. Nanophotonics. 2018;7(10):1637. https://doi.org/10.1515/nanoph-2018-0117.
[92] Grosso BF, Mele EJ. Bending rules in graphene kirigami. Phys Rev Lett. 2015;115(19):195501. https://doi.org/10.1103/PhysRevLett.115.195501.
[93] Castle T, Cho Y, Gong X, Jung E, Sussman DM, Yang S, Kamien RD. Making the cut: lattice kirigami rules. Phys Rev Lett. 2014;113(24):245502.
[94] Han X, Seo KJ, Qiang Y, Li ZP, Vinnikova S, Zhong YD, Zhao XY, Hao PJ, Wang SD, Fang H. Nanomeshed Si nanomembranes. npj Flex Electron. 2019;3(1):9. https://doi.org/10.1038/s41528-019-0053-5.
[95] Liu SJ, Li L, Hao YP, Diao XL, Liu FL. Optimization of positioning technology of aspheric compound eyes with variable focal length. AIP Adv. 2019;9(1):015133. https://doi.org/10.1063/1.5032268.
[96] Li L, Hao YP, Xu JL, Liu FL, Lu J. The design and positioning method of a flexible zoom artificial compound eye. Micromachines. 2018;9(7):319. https://doi.org/10.3390/mi9070319.
[97] Luan SY, Cao H, Deng HF, Zheng GX, Song Y, Gui CQ. Artificial hyper compound eyes enable variable-focus imaging on both curved and flat surfaces. ACS Appl Mater Interfaces. 2022;14(40):46112. https://doi.org/10.1021/acsami.2c15489.
[98] Liu YK, Zhang CY, Kou TD, Li YY, Shen JF. End-to-end computational optics with a singlet lens for large depth-of-field imaging. Opt Express. 2021;29(18):28530. https://doi.org/10.1364/OE.433067.
[99] Gál J, Horváth G, Clarkson ENK, Haiman O. Image formation by bifocal lenses in a trilobite eye? Vision Res. 2000;40(7):843. https://doi.org/10.1016/S0042-6989(99)00216-3.
[100] Liu XQ, Yang SN, Yu L, Chen QD, Zhang YL, Sun HB. Rapid engraving of artificial compound eyes from curved sapphire substrate. Adv Funct Mater. 2019;29(18):1900037. https://doi.org/10.1002/adfm.201900037.
[101] Tanida J, Kumagai T, Yamada K, Miyatake S, Ishida K, Morimoto T, Kondou N, Miyazaki D, Ichioka Y. Thin observation module by bound optics (TOMBO): concept and experimental verification. Appl Opt. 2001;40(11):1806. https://doi.org/10.1364/ao.40.001806.
[102] Duparre J, Wippermann F, Dannberg P, Reimann A. Chirped arrays of refractive ellipsoidal microlenses for aberration correction under oblique incidence. Opt Express. 2005;13(26):10539. https://doi.org/10.1364/opex.13.010539.
[103] Li L, Yi AY. Development of a 3D artificial compound eye. Opt Express. 2010;18(17):18125. https://doi.org/10.1364/OE.18.018125.
[104] Wang YY, Shi CY, Liu CY, Yu XD, Xu HR, Wang TS, Qiao YF, Yu WX. Fabrication and characterization of a polymeric curved compound eye. J Micromech Microeng. 2019;29(5):055008. https://doi.org/10.1088/1361-6439/ab0e9f.
[105] Deng ZF, Chen F, Yang Q, Bian H, Du GQ, Yong JL, Shan C, Hou X. Dragonfly-eye-inspired artificial compound eyes with sophisticated imaging. Adv Funct Mater. 2016;26(12):1995. https://doi.org/10.1002/adfm.201504941.
[106] Su SJ, Liang JS, Li XJ, Xin WW, Ye XS, Xiao JP, Xu J, Chen L, Yin PH. Hierarchical artificial compound eyes with wide field-of-view and antireflection properties prepared by nanotip-focused electrohydrodynamic jet printing. ACS Appl Mater Interfaces. 2021;13(50):60625. https://doi.org/10.1021/acsami.1c17436.
[107] Wu D, Wang JN, Niu LG, Zhang XL, Wu SZ, Chen QD, Lee LP, Sun HB. Bioinspired fabrication of high-quality 3D artificial compound eyes by voxel-modulation femtosecond laser writing for distortion-free wide-field-of-view imaging. Adv Opt Mater. 2014;2(8):751. https://doi.org/10.1002/adom.201400175.
[108] Kuo WK, Lin SY, Hsu SW, Yu HH. Fabrication and investigation of the bionic curved visual microlens array films. Opt Mater. 2017;66:630. https://doi.org/10.1016/j.optmat.2017.03.020.
[109] Kuo WK, Kuo GF, Lin SY, Her YuH. Fabrication and characterization of artificial miniaturized insect compound eyes for imaging. Bioinspir Biomim. 2015;10(5):056010. https://doi.org/10.1088/1748-3190/10/5/056010.
[110] Liu HW, Chen F, Yang Q, Qu PB, He SG, Wang XH, Si JH, Hou X. Fabrication of bioinspired omnidirectional and gapless microlens array for wide field-of-view detections. Appl Phys Lett. 2012;100(13):133701. https://doi.org/10.1063/1.3696019.
[111] Charman WN, Tucker J. The optical system of the goldfish eye. Vision Res. 1973;13(1):1. https://doi.org/10.1016/0042-6989(73)90160-0.
[112] Ma MC, Li H, Gao XC, Si WH, Deng HX, Zhang J, Zhong X, Wang KY. Target orientation detection based on a neural network with a bionic bee-like compound eye. Opt Express. 2020;28(8):10794. https://doi.org/10.1364/oe.388125.
[113] Xu HR, Zhang YJ, Wu DS, Zhang G, Wang ZY, Feng XP, Hu BL, Yu WX. Biomimetic curved compound-eye camera with a high resolution for the detection of distant moving objects. Opt Lett. 2020;45(24):6863. https://doi.org/10.1364/ol.411492.
[114] Wang SK, Zhang F, Yang Q, Li MJ, Hou X, Chen F. Chalcogenide glass IR artificial compound eyes based on femtosecond laser microfabrication. Adv Mater Technol. 2023;8(2):2200741. https://doi.org/10.1002/admt.202200741.
[115] Stockman A, Sharpe LT. Human cone spectral sensitivities and color vision deficiencies. Vis Transduct Non-Vis Light Percept. 2008. https://doi.org/10.1007/978-1-59745-374-5_14.
[116] Cronin TW, Porter ML, Bok MJ, Caldwell RL, Marshall J. Colour vision in stomatopod crustaceans. Phil Trans R Soc B. 1862;2022(377):20210278. https://doi.org/10.1098/rstb.2021.0278.
[117] Liu F, Bian H, Zhang F, Yang Q, Shan C, Li MJ, Hou X, Chen F. IR artificial compound eye. Adv Opt Mater. 2020;8(4):1901767. https://doi.org/10.1002/adom.201901767.
[118] Wu WQ, Lu H, Han X, Wang CF, Xu ZS, Han ST, Pan CF. Recent progress on wavelength-selective perovskite photodetectors for image sensing. Small Methods. 2023;7:2201499. https://doi.org/10.1002/smtd.202201499.
[119] Zhou FC, Zhou Z, Chen JW, Choy TH, Wang JL, Zhang N, Lin ZY, Yu SM, Kang JF, Wong HSP, Chai Y. Optoelectronic resistive random access memory for neuromorphic vision sensors. Nat Nanotechnol. 2019;14(8):776. https://doi.org/10.1038/s41565-019-0501-3.
[120] Zhu QB, Li B, Yang DD, Liu C, Feng S, Chen ML, Sun Y, Tian YN, Su X, Wang XM, Qiu S, Li QW, Li XM, Zeng HB, Cheng HM, Sun DM. A flexible ultrasensitive optoelectronic sensor array for neuromorphic vision systems. Nat Commun. 2021;12(1):1798. https://doi.org/10.1038/s41467-021-22047-w.
[121] Lee TJ, Yun KR, Kim SK, Kim JH, Jin J, Sim KB, Lee DH, Hwang GW, Seong TY. Realization of an artificial visual nervous system using an integrated optoelectronic device array. Adv Mater. 2021;33(51):2105485. https://doi.org/10.1002/adma.202105485.
[122] Mennel L, Symonowicz J, Wachter S, Polyushkin DK, Molina-Mendoza AJ, Mueller T. Ultrafast machine vision with 2D material neural network image sensors. Nature. 2020;579(7797):62. https://doi.org/10.1038/s41586-020-2038-x.
[123] Han X, Xu ZS, Wu WQ, Liu XH, Yan PG, Pan CF. Recent progress in optoelectronic synapses for artificial

visual-perception system. Small Struct. 2020;1(3):2000029. https://doi.org/10.1002/sstr.202000029.
[124] Jia MM, Guo PW, Wang W, Yu AF, Zhang YF, Wang ZL, Zhai JY. Tactile tribotronic reconfigurable p-n junctions for artificial synapses. Sci Bull. 2022;67(8):803. https://doi.org/10.1016/j.scib.2021.12.014.
[125] Teng CJ, Yu QM, Sun YJ, Ding BF, Chen WJ, Zhang ZH, Liu BL, Cheng HM. Homologous gradient heterostructure-based artificial synapses for neuromorphic computation. InfoMat. 2023;5(1):e12351. https://doi.org/10.1002/inf2.12351.
[126] Yan YL, Yu NN, Yu ZY, Su YP, Chen JW, Xiang T, Han YN, Wang JF. Optoelectronic synaptic memtransistor based on 2D SnSe/MoS_2 van der Waals heterostructure under UV–ozone treatment. Small Methods. 2023;7:2201679. https://doi.org/10.1002/smtd.202201679.
[127] Zhang C, Li Y, Ma CL, Zhang QC. Recent progress of organic-inorganic hybrid perovskites in rram, artificial synapse, and logic operation. Small Sci. 2022;2(2):2100086. https://doi.org/10.1002/smsc.202100086.
[128] Sun YL, Li MJ, Ding YT, Wang HP, Wang H, Chen ZM, Xie D. Programmable van-der-Waals heterostructure-enabled optoelectronic synaptic floating-gate transistors with ultra-low energy consumption. InfoMat. 2022;4(10):e12317. https://doi.org/10.1002/inf2.12317.
[129] Choi C, Leem J, Kim M, Taqieddin A, Cho C, Cho KW, Lee GJ, Seung H, Bae HJ, Song YM, Hyeon T, Aluru NR, Nam S, Kim DH. Curved neuromorphic image sensor array using a MoS_2-organic heterostructure inspired by the human visual recognition system. Nat Commun. 2020;11(1):5934. https://doi.org/10.1038/s41467-020-19806-6.
[130] Hu YX, Dai MJ, Feng W, Zhang X, Gao F, Zhang SC, Tan BY, Zhang J, Shuai Y, Fu YQ, Hu PA. Ultralow power optical synapses based on MoS_2 layers by indium-induced surface charge doping for biomimetic eyes. Adv Mater. 2021;33(52):2104960. https://doi.org/10.1002/adma.202104960.
[131] Chen JG, Cao GM, Liu Q, Meng P, Liu Z, Liu FC. Two-dimensional Nb_3Cl_8 memristor based on desorption and adsorption of O_2 molecules. Rare Met. 2022;41(1):325. https://doi.org/10.1007/s12598-021-01794-1.
[132] Chao YH, Chen JC, Yang DL, Tseng YJ, Hsu CH, Chen JY. High-performance non-volatile flash photomemory via highly oriented quasi-2D perovskite. Adv Funct Mater. 2022;32(19):2112521. https://doi.org/10.1002/adfm.202112521.
[133] Yang YF, Chiang YC, Lin YC, Li GS, Hung CC, Chen WC. Highly efficient photo-induced recovery conferred using charge-transfer supramolecular electrets in bistable photonic transistor memory. Adv Funct Mater. 2021;31(40):2102174. https://doi.org/10.1002/adfm.202102174.
[134] Wang Y, Iglesias D, Gali SM, Beljonne D, Samorì P. Light-programmable logic-in-memory in 2D semiconductors enabled by supramolecular functionalization: photoresponsive collective effect of aligned molecular dipoles. ACS Nano. 2021;15(8):13732. https://doi.org/10.1021/acsnano.1c05167.
[135] Shi N, Zhang J, Ding Z, Jiang H, Yan Y, Gu D, Li W, Yi MD, Huang FZ, Chen SF, Xie LH, Ren YB, Li Y, Huang W. Ultrathin metal-organic framework nanosheets as nano-floating-gate for high performance transistor memory device. Adv Funct Mater. 2022;32(12):2110784. https://doi.org/10.1002/adfm.202110784.
[136] Liu JH, Zhang ZC, Qiao S, Fu GS, Wang SF, Pan CF. Lateral bipolar photoresistance effect in the CIGS heterojunction and its application in position sensitive detector and memory device. Sci Bull. 2020;65(6):477. https://doi.org/10.1016/j.scib.2019.11.016.
[137] Zou LR, Sang DD, Yao Y, Wang XT, Zheng YY, Wang NZ, Wang C, Wang QL. Research progress of optoelectronic devices based on two-dimensional MoS_2 materials. Rare Met. 2023;42(1):17. https://doi.org/10.1007/s12598-022-02113-y.
[138] Zhang XM, Lu J, Wang ZR, Wang R, Wei JS, Shi T, Dou CM, Wu ZH, Zhu JX, Shang DS, Xing GZ, Chan MS, Liu Q, Liu M. Hybrid memristor-CMOS neurons for in-situ learning in fully hardware memristive spiking neural networks. Sci Bull. 2021;66(16):1624. https://doi.org/10.1016/j.scib.2021.04.014.
[139] Yang L, Huang XD, Li Y, Zhou HJ, Yu YJ, Bao H, Li JC, Ren SG, Wang F, Ye L, He YH, Chen J, Pu GY, Li X, Miao XS. Self-selective memristor-enabled in-memory search for highly efficient data mining. InfoMat. 2023;5:e12416. https://doi.org/10.1002/inf2.12416.
[140] Xu JQ, Zhao XN, Zhao XL, Wang ZQ, Tang QX, Xu HY, Liu YC. Memristors with biomaterials for biorealistic neuromorphic applications. Small Sci. 2022;2(10):2200028. https://doi.org/10.1002/smsc.202200028.
[141] Kim Y, Zhu C, Lee WY, Smith A, Ma H, Li X, Son D, Matsuhisa N, Kim J, Bae WG, Cho SH, Kim M-G, Kurosawa T, Katsumata T, To JWF, Oh JY, Paik S, Kim SJ, Jin L, Yan F, Tok JBH, Bao Z. A hemispherical image sensor array fabricated with organic photomemory transistors. Adv Mater. 2023;35(1):2203541. https://doi.org/10.1002/adma.202203541.